Surface Reconstruction using Multipath Propagation in Indoor MIMO Radar

Jakob Henningsson, Elias Olson

Master's thesis
2023:E41

Lund University

Faculty of Engineering
Centre for Mathematical Sciences
Mathematical Statistics

CENTRUM SCIENTIARUM MATHEMATICARUM

Master’s Theses in Mathematical Sciences 2023:E41
ISSN 1404-6342

LUTFMS-3479-2023

Mathematical Statistics
Centre for Mathematical Sciences
Lund University
Box 118, SE-221 00 Lund, Sweden

http://www.maths.lu.se/

EXAMENSARBETE
Matematisk Statistik

LU-CS-EX: 2023-79

Surface Reconstruction using Multipath Propagation in Indoor MIMO Radar

Rekonstruktion av Reflekterande Ytor i Inomhusmiljö med MIMO-radar

Jakob Henningsson, Elias Olson

Surface Reconstruction using Multipath Propagation in Indoor MIMO Radar

Jakob Henningsson
`ja7241he-s@student.lu.se`

Elias Olson
`el4180ol-s@student.lu.se`

June 1, 2023

Supervisors: Anders Mannesson
Santhosh Nadig
Andreas Jakobsson

Examiner: Ted Kronwall

Abstract

Using active radar for localization in indoor environments is challenging. By signal reflection off walls and other static objects, false targets occur, referred to as multipath "ghosts". These are a significant hinder in interpreting the data. For this reason mapping out problematic surfaces that produce reflections is an important task, preferably without prior knowledge of the room geometry.

For multiple-input multiple-output(MIMO) radar a solution utilizing a linear relationship in range-Doppler in order to classify the multipath ghosts, has been investigated previously. The focus was mainly on simulated data. Additionally, reconstruction of the reflecting surfaces, using the multipath propagation, has been done on solely simulated data. In this thesis we propose a similar solution, utilizing the linear relationship, adapted to handle real data. Particularly, reconstructing the reflecting surfaces is in focus.

The aim of this thesis is to evaluate the solution in a range of scenarios, assessing its capacity to correctly reconstruct reflective surfaces. It is shown to handle varying angled single walls with good results. Scenes with multiple walls has also been investigated, showing promising results. With the reflective surfaces in a scene mapped, this can for example be used to designate areas where only multipath signals will occur, making it possible for these to be filtered out and ignored. The thesis has focused on human targets, but the solution has potential to be applicable in automotive scenarios as well, where the same linear relationship should be present.

Keywords: Multiple-input multiple-output (MIMO) radar, multipath recognition, geometry reconstruction

Acknowledgements

First off, we would like to thank our industry supervisors Andreas Mannesson and Santhosh Nadig for all their insights, assisting us with everything from smaller to bigger issues, as well as making us feel very welcome and included in the team. Secondly, we would like to thank our supervisor at Lund University, Andreas Jakobsson for his valuable feedback and quick response to any questions.

Contents

Chapter 1

Introduction

1.1 Background

Indoor radar use is an emerging field due to its privacy-friendly nature. In scenarios where a camera is traditionally used, a radar offers increased privacy while performing many of the same tasks as the camera. When mounting a radar in an indoor environment there is often an abundance of reflecting surfaces like walls, floor and other objects. In the presence of these surfaces, new paths open up for the signal to bounce. These new signal paths cause what is called multipath detections in radar communications. Multipath detections may cause ghost targets which are duplicates of the target in a scene, and these ghosts may in turn generate a ghost track. Such ghost tracks cause confusion, misclassification and misrepresent what is actually happening in the scene. The placement of these multipath detections is dependent on the following:

1. The position of the target in the scene.
2. The position and orientation of the reflecting surface causing the multipath to occur.

1.2 Purpose

The aim of this thesis is to explore methods to identify multipath detections as well as use the identified detections to estimate where the reflective surface in question is situated. The data that will be used is solely real data. The thesis also aims to investigate how the performance of such a method is affected by the placement of the reflective surfaces in relation to the radar, and the path taken by the target. In this thesis we have restricted the scenes to contain simple geometries, which means that curved objects and scenes cluttered with reflective surfaces are not investigated. The reflective surfaces that are present will be limited to walls only and the multipath model will hence be in two dimensions. We have also restricted the problem to one target. With this background, the goal of the thesis is to answer the following questions:

- Can a single reflecting wall be accurately mapped?
- Does the angle of the wall impact the results?
- Introducing an additional reflecting wall, can both walls be accurately reconstructed?

1.3 Prior Work

Multipath reflections in radar is a field that has been studied in a range of articles. A selection of these are presented below. In 1.3.1 ray tracing approaches are discussed. Common with these are that a prior geometry knowledge is demanded. Section 1.3.2 and 1.3.3 contain approaches that in contrast does not require prior geometry information. In 1.3.2 machine learning is the focus, while in 1.3.3 a relationship in range-Doppler is the focus, from which this thesis borrows many ideas. Note that range is the distance to the radar and Doppler means the radial velocity. How these are estimated by the radar will be explained in *Chapter 2*.

1.3.1 Ray Tracing

Setlur et al.[1] has used ray tracing methods to map multipath points to the real target for a through-the-wall radar. Ray tracing is a method for analysing the path of the signal when propagating through the system of interest. The rays are narrow idealized beams, that are systematically propagated through the system and surface reflection etc. can be simulated[2]. The goal of the article was to eliminate ghosts but at the same time use the ghost points to increase signal-to-clutter(SCR) ratio for the real targets, i.e. make them more distinct compared to the noisy background. With this approach they assumed a known geometry and target location. In evaluating their algorithm they used both simulations and real radar data.

Multipath in an automotive scenario has been investigated by Kamann et al[3], also using ray tracing. In their article they do a purely geometrical derivation of where the different reflections will occur, given a known reflector position and with a sensor moving at a known curve. This can also be expressed as finding a relationship in the range-angle domain, where range as mentioned earlier is the distance to the radar. Range and angle combined is equivalent to the (x,y) coordinates. This solution was first used to estimate the reflection positions of an experimental target, paired with a highway barrier as the reflecting surface. In order to show applicability to real world scenarios the solution was also tried on a real vehicle as target, paired with a building wall as reflector.

A third example utilizing ray tracing is a solution developed by Thai et al.[4], that aims to detect and localize hidden objects by way of the multipath reflections. This is referred to as around-the-corner radar (ACR). The solution is showing promising numerical results. As mentioned for previous examples, ray tracing demands a prior knowledge of the geometry. In the article they propose that rough map information, often possible to be retrieved in automotive scenarios, can cover this need of prior geometry knowledge. Test runs on real experimental data shows indication that this can suffice to retrieve target position of hidden targets.

1.3.2 Machine Learning

Krauss et al.[5] has done a classifier on real vs multipath points using machine learning. The work was restricted to annotate certain multipath points, which they refer to as third-bounce reflections of type-2. These are points that first hit the reflective surface, then the real target and finally the reflective surface again before travelling back to the radar. In this thesis these are referred to as second order ghosts. In other words they restricted their work to distinguish between this category of multipath reflections and real radar hits. The machine learning network used was the PointNet++ architecture, described as an end-to-end neural network architecture, directly processing radar point clouds.

1.3.3 Classification in Range-Doppler and Geometry Estimation

Feng et al. [6] has in their article *Multipath Ghost Recognition for Indoor MIMO Radar* the main focus of implementing a classifier for multipath detections, in the range-Doppler domain. Remember that range is the distance of the object to the radar and Doppler represents the radial velocity, which both are estimated with a radar. The radar they use is a MIMO-radar, similar to the one used in this thesis. MIMO is an acronym for multiple-input multiple-output, meaning a use of several transmitting and receiving antennas. This concept will be explained further in *Chapter 2*. The radar is run with ultra-wideband configuration, making the range resolution enhanced, i.e. possible to discern targets from one another at smaller intertarget distances. This classifier is based on a linear relationship between the ghost targets in range-Doppler, which they have derived. Compared to the ray tracing approaches of [1], this solution does not require prior knowledge of the geometry. A big part of their work is performed on simulated radar data, but they evaluate on experimental data as well. In addition to classifying ghosts, they present a figure of wall estimation based on the classification. The wall estimation is done with simulated data. This thesis draws big inspiration from their work and intends to implement a similar algorithm, but with heavier focus on the wall estimation side. In this thesis, the focus will be solely on real radar data.

In *Multipath Ghost Classification for MIMO Radar Using Deep Neural Networks* [7] Feng et. al. further develops their algorithm by adding a Deep Neural Network (DNN) classification step which has the purpose of classifying a detection as having the same direction-of-departure (DoD) as direction-of-arrival (DoA) of the signal, versus having different DoD and DoA. The direction-of-departure is the direction the signal traveled to reach the target, and the direction-of-arrival is the direction it returned from the target. In their geometric multipath model, targets and second order ghosts(two reflections in wall) have the same DoD as DoA, while first order ghosts(one reflection in wall) do not. The geometric multipath model is used in this thesis also, and is explained further in 2.2. Extending their solution with the DNN classification step, they were able to classify detections to a high degree of certainty for both simulated and real data.

Chapter 2
Theory

In this chapter key theory concepts related to this thesis are presented. The radar provided for the thesis is an active radar, meaning that it transmits its own signal, not just listens to signals in its surrounding as is the case with passive radar[8]. The type of the radar was FMCW, hence its principles are first explained in 2.1. This is followed by an explanation of the geometry of the multipath signals in 2.2, that has been in focus in this thesis. A linear relationship between different multipath reflections is introduced in 2.3, derived by Feng et al[6]. In 2.4 a popular algorithm for finding lines in images is explained. The way of finding the lines in 2.3 is based on this algorithm. In 2.5 the clustering used to separate segments, originating from different reflections, is described. The chapter is ended in 2.6 with an introduction to a possible problem with estimating the angle of one type of reflections.

2.1 FMCW Radar

The work done in this thesis was carried out on a Frequency Modulated Continous Wave (FMCW) radar. As the name suggests, it transmits a continuous signal, in contrast to pulsed radar. FMCW radar is state-of-the-art for applications within the automotive industry[9]. The technique is also used in the surveillance industry, complementing the visual camera with both position and speed information, in addition to being resilient to low-light scenarios and occluding weather[10]. Compared to pulsed radar, FMCW can achieve advantageous range and velocity resolutions, without as high cost or complexity[11]. Three quantities are of interest to estimate with the radar: range, velocity(radial) and direction[12]. These estimations will be explained in turn in the following sections.

2.1.1 Range Estimation

The idea of estimating range is simply to send out a signal and count how long it takes for it to bounce off the target and return to the radar. In order to measure this round-trip delay, start and stop marks in the signal are needed. For continuous radar this is done with frequency modulated so called chirps[12]. This means that the signal is composed out of short packages of typically tens of microseconds[13], where the frequency is linearly increasing(or decreasing). Effectively this creates start and stop reference points, against which the signal coming back can be compared. Figure 2.1 shows these transmitted chirps alongside received chirps, returning after a time delay τ as a result of reflection off a target. Several transmitted and received chirps are shown, which are later needed for the velocity estimation. The interval between lowest and highest frequency of the chirps is referred to as the bandwidth(B), and is directly associated with the range resolution, i.e. the smallest difference in distance the radar can measure. The slope of the chirps, designated with S, fulfill the relationship[13]

$$S = \frac{B}{T}, \tag{2.1}$$

where T is the duration of the chirp, also named modulation time. Typically a bandwidth in the hundreds of MHz is used. As mentioned, the modulation time is typically in the tens of microseconds[13].

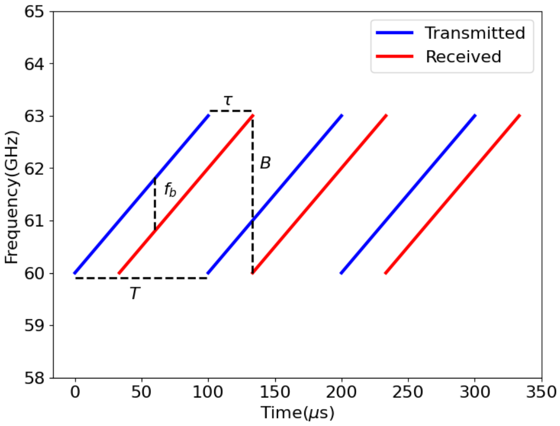

Figure 2.1: Transmitted and received chirps used by an FMCW radar. T is the chirp duration, f_b is the beat frequency, B is the bandwidth and τ is the time delay between transmitted and received chirp.

Estimation of the range can be done using a single chirp. Instead of measuring the time delay between transmitted and received chirp, τ in figure 2.1, the difference in frequency f_b is instead measured. The difference in frequency is referred to as the beat frequency. This is identified from mixing the signals, i.e. multiplying the transmitted and received signals. Suleymanov [13] derives an approximate expression for the mix of the n^{th} chirp as

$$x_m(t_s, n) = \frac{A_t A_r}{2} \cos\left[2\pi \left(\frac{2SR}{c} t_s + \frac{2 f_c D n}{c} T\right) + \frac{4\pi f_c R}{c}\right]. \tag{2.2}$$

In equation 2.2 t_s is the time from the start of the n^{th} chirp, A_t and A_r are the amplitudes of the transmitted and received signal respectively, S is the chirp slope, R is the target range, c is the speed of light, f_c is the starting frequency of the chirps and D is the radial velocity of the target, also called its Doppler-speed. Out of these parameters, the range R and the Doppler-speed D are the unknowns. Hence the goal is to estimate these with the radar. In the derivation by Suleymanov, only the low-frequency component of the mixed signal is included, corresponding to the beat frequency f_b. The higher frequency part is filtered out in the radar system[13]. For a single chirp, the range term $\frac{2SR}{c}t_s$ in equation 2.2 will be dominating. This can be verified by inserting typical values for the quantities, resulting in a magnitude much greater than for the Doppler-term $\frac{2f_cDn}{c}T$. Note that the third term $\frac{4\pi f_cR}{c}$ is a constant phase term. With this background, the beat frequency for a single chirp can be said to be directly related to the range-term[13]:

$$f_b = \frac{2SR}{c}. \tag{2.3}$$

Like most applications where the task is to identify frequencies in a signal, a fast Fourier transform(FFT) is used to retrieve the beat frequency[13]. This is often referred to as the range-FFT or fast-time FFT[12], since it is done over a short time domain, a single chirp. So with the beat frequency identified, the range follows from equation 2.3. The range resolution is the minimum range that the radar can distinguish two targets[14].It can be derived to be inversely dependent on the bandwidth[13]:

$$\Delta R = \frac{c}{2B}. \tag{2.4}$$

2.1.2 Velocity Estimation

Estimating velocity in a radar is based on the Doppler shift, where a moving target alters the frequency of the signal. Only movements towards or away from the radar, i.e. in the radial direction, compresses or elongates the signal. In other words, the velocity we are estimating is in fact the radial velocity, but will simply be referred to as velocity[12]. The velocity estimation is, in contrast to the range estimation, done over a collection of M chirps. Once here, the range has been estimated on each chirp, as explained in the previous section. After M chirps have been collected and saved, the velocity can be estimated. This is visualised in figure 2.2, where targets are marked with different colors. The collection of M chirps is often referred to as a frame[12]. Each chirp is very short, tens of microseconds or so, making the duration of the frame comparably short as well, with M being chosen in the range of hundreds[13]. The short frame duration makes it a valid assumption that the target is on a constant range throughout the frame, at least when not observing very high speed targets[12]. This is seen in figure 2.2, with both clusters of targets, later separated in Doppler, staying on the same range for all chirps[12].

Recalling the expression for the mixed signal(eq. 2.2), a constant range implies that the velocity term $\frac{2f_cv}{c} \cdot nT$ will be the only one altering the phase between chirps. This phase, varying linearly with the chirp n, corresponds to the target Doppler frequency f_d. It is illustrated in figure 2.3. Expressing it using the velocity term we get

$$f_d = \frac{2f_cv}{c}, \tag{2.5}$$

and hence the velocity v can be directly retrieved from this frequency[13]. Estimating the frequency is done with a second FFT, the Doppler-FFT. It is also referred to as slow-time FFT, since it is performed over a larger time domain than the range-FFT, several chirps. Figure 2.2 shows how targets sharing the same range are separated after the Doppler-FFT[12]. With the

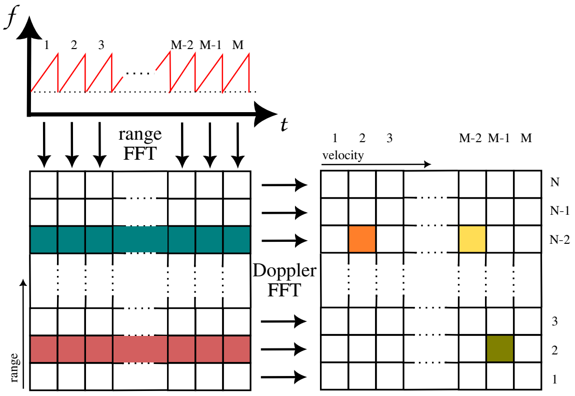

Figure 2.2: Visualization of the range- and Doppler-FFTs. The colorized parts represent targets in the scene. Two of them are on the same range and are resolved after the Doppler-FFT.

information from the range-FFT and Doppler-FFT, the so called range-Doppler map can be constructed. An example of this is seen in figure 2.4.

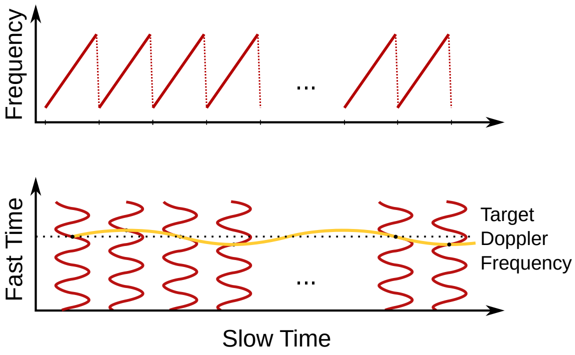

Figure 2.3: Phase difference across chirps, corresponding to the Doppler shift caused by the relative velocity of the target in relation to the radar. Together these phase differences compose a frequency, used to estimate the target velocity.

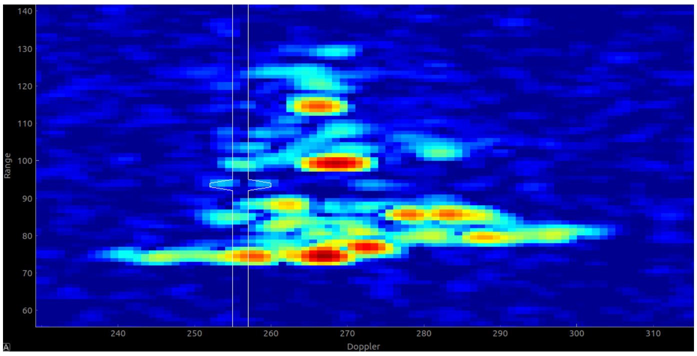

Figure 2.4: Example of a range-Doppler map.

2.1.3 Angle Estimation

So far we have discussed the process in which an FMCW radar produces the range and velocity information of a target. For this to be really useful one needs to know in which direction the target is as well. In this thesis multiple-input multiple-output radar has been used for this.

Multiple-Input Multiple-Output

One way of approaching angle estimation is to use multiple transmitting(TX) and receiving(RX) antennas. This approach is called multiple-input multiple-output radar or MIMO radar for short. The principle is very similar to the velocity estimation over chirps. Here a phase difference is also utilized, but this time between antennas instead of between chirps. Under the assumption that the signal has traveled so far that it is a plane wave when reaching the receiving antennas, the phase shift can easily be worked out geometrically. This is illustrated in figure 2.5 between two receiving antennas, from which the following relationship for the phase shift can be derived[15]:

$$\Delta\psi = \frac{2\pi d \sin\theta}{\lambda}, \tag{2.6}$$

where d is the interantenna distance, θ is the incident angle compared to the forward direction of the radar, often referred to as boresight, and λ is the wavelength of the signal. Solving for the angle gives:

$$\theta = \arcsin \frac{\Delta\psi\lambda}{2\pi d}. \tag{2.7}$$

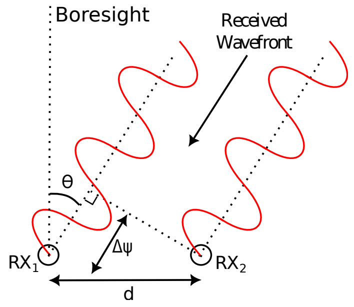

Figure 2.5: Phase shift $\Delta\psi$ of plane wave received by two receivers, with an incident angle of θ compared to the boresight of the radar.

In order to make the angle estimation more robust, more receiving antennas than two are often added. Four receivers are a typical number, although often coupled with more than one transmitter, effectively functioning as having even more receivers(will be discussed shortly). With $N_{TX} = 1$ and $N_{RX} = 4$ receivers placed with an equal interantenna distance of d, the phase differences will be linearly increasing in relation to the first one as $[0, \Delta\psi, 2\Delta\psi, 3\Delta\psi]$. An increased number of receivers also positively affects the angular resolution[15]. The case with $N_{TX} = 1$ and $N_{RX} > 1$ is in fact a multiple-input single-output(MISO) setup.

As mentioned earlier, adding more transmitters, making the radar multiple-input multiple-output(MIMO), is a way of increasing the number of phase differences to work with. Together the transmitters and receivers construct a so called virtual array with $N_{TX} \cdot N_{RX}$ elements. A typical example is using $N_{TX} = 2$ transmitters and $N_{RX} = 4$ receivers, which was the setup of the provided radar used in this thesis. This results in a virtual array of size 8. To achieve linearly increasing phase differences the transmitters need to be appropriately placed, for example with an interantenna distance of $4d$, but other placements are possible. This is illustrated in figure 2.6. Note that the transmitted signal is a circular wave-front, the arrows indicate the part of the wave-front reflecting of a target in the direction of θ and returning to the radar. The signal transmitted from the second transmitter will have to travel a distance of $4d \sin\theta$ extra, resulting in a phase shift of an additional $4\Delta\psi$ compared to the first transmitter. In total we get 8 linearly increasing phase differences $[0, \Delta\psi, 2\Delta\psi, 3\Delta\psi, 4\Delta\psi, 5\Delta\psi, 6\Delta\psi, 7\Delta\psi]$, with the latter half originating from the transmitter with longer path to the target[15].

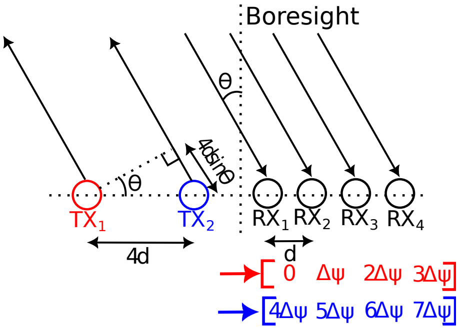

Figure 2.6: Set of phase shifts produced by two transmitters and four receivers. The incident angle of the wave is θ compared to the radar boresight.

A necessity for the MIMO concept to work is that the signals from the different transmitters can be separated. There is a couple ways of approaching this problem, but the approach used in our setup is the one called time division multiplexing. Therefore we will restrict us to explaining this.

Time Division Multiplexing

The principle of time division multiplexing is quite simple. The TXs take turns transmitting. This is done on a chirp basis, i.e. each TX gets to transmit one chirp before the next takes over. An example in the case $N_{TX} = 2$ is shown in figure 2.7. The 2D-FFTs discussed earlier, range-FFT(fast-time) and Doppler-FFT(slow-time), resulting in a range-Doppler map is done on each TX/RX pair, which is the same as each element in the virtual array[15]. These elements are often referred to as channels. In total this produces $N_{TX} \cdot N_{RX}$ number of range-Doppler maps. To fetch the angular information another FFT is run across these maps, i.e. across the channels. This is referred to as the angle-FFT. So in total 3 FFTs are used to retrieve range, velocity and angle, resulting in a cube of information[16]. This process is summarized in figure 2.8.

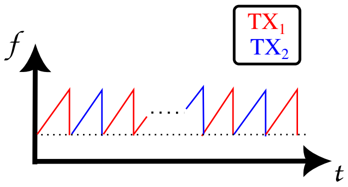

Figure 2.7: Illustration of time division multiplexing with two transmitting antennas.

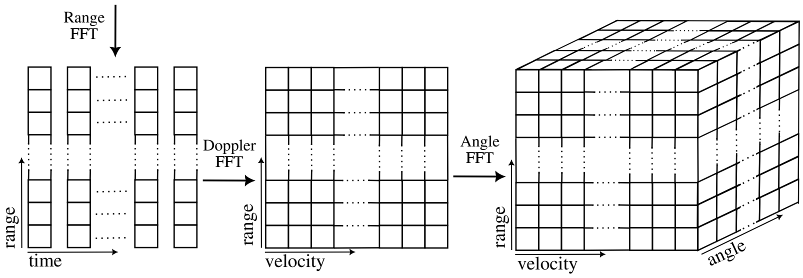

Figure 2.8: Three FFTs estimating the three radar quantities(range, velocity, angle).

2.2 Multipath Signals

Multipath detections occur in a scene when the signal may not only travel from radar, to target, and back to the radar, but may also travel by way of a reflective surface. These reflective surfaces can be any object that causes another path to be available to the signal. For example a signal received via reflection in a wall, is interpreted by the radar as a target located in the direction of the reflection, and on the range of half the total signal path. This due to the radar assuming that the signal traveled the direct path to the target and back. The consequences of this is that detections might appear inside a wall, although obviously no real target is located there. These detections are often referred to as "ghost targets" or simply "ghosts"[6]. An example showing that this is in fact what we see in practice is shown in figure 2.9, where a lot of detections are occurring inside a wall. These are problematic when interpreting the data you receive from the radar.

The radar signal geometry when reflecting in the wall **P** is shown in figure 2.10[6]. In the following theory describing the properties of the multipath reflections, a couple of assumptions are made. The target in question is assumed to be a point which spreads the signal in all directions. The wall **P** is on the other hand assumed to be a perfectly plane reflector, causing the signal to reflect with the same angle as the angle of incidence. In figure 2.10 several new paths are available to the signal. The direct path **OT-TO** is from the radar **O** to the target **T** and back. This is what results in the real target detection. A new path **OP-PT-TO** is available which bounces once in the wall **P**. This path is expressed using blue arrows in figure 2.10. The path results in a so called "ghost target" or simply "ghost, i.e. detections appearing at a position not corresponding to a real object. This particular ghost appears behind the target **T**, due to that the Direction of Arrival (DoA) to the radar is the same as **T**, but the signal has traveled further. This ghost will be referred to as **M2**. The same path in the opposite direction **OT-TP-PO** will also result in a ghost which will be referred to as **M1**. **M1** is on the same range as **M2** due to it having the same signal path but backwards. The DoA of **M1** will

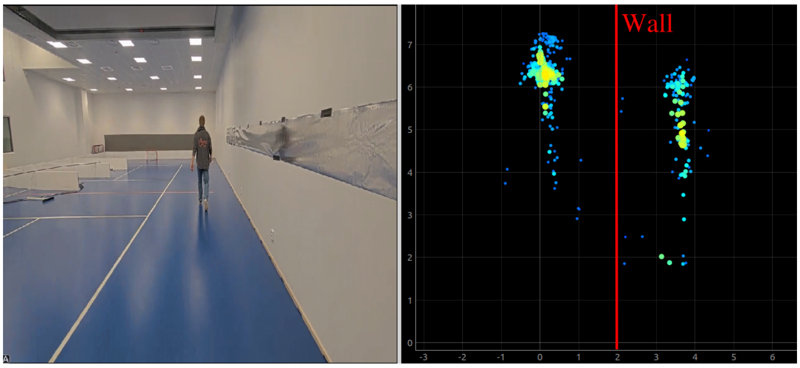

Figure 2.9: Example scene showing ghost detections occurring inside the wall due to reflections. Camera perspective to the left and top-down view to the right, showing significant number of detections at the actual target position as well as inside the wall.

contrary to **M2** not be the same as **T**. Instead **M1** will appear behind the wall segment **P** in which it was reflected. **M1** and **M2** are collectively referred to as first order ghosts since they arose due to a singular reflection in the wall. This multipath model also contains a second order ghost **S**, taking the signal path **OP-PT-TP-PO**. This path contains two reflections in the same wall segment. The DoA of **S** is the same as **M1**, causing **S** to appear behind the wall, but on a larger range compared to **M1**.

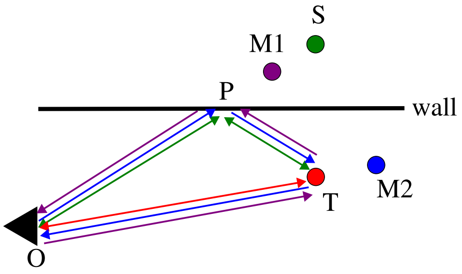

Figure 2.10: Multipath geometry when the radar reflects in a wall.

2.3 Linear Relationship in Range-Doppler

With the background in section 2.2, reflections of the radar signal result in a range of "ghosts". It is of interest to classify which is which, in particular which targets are real and which are ghosts. Feng et al. [6] derive a relationship between them in the range-Doppler domain, suitable for this purpose. First off, the range of the target is expressed as

$$R_T = \frac{R_{OT} + R_{TO}}{2}, \tag{2.8}$$

with the symbols from figure 2.10. The range of the second order ghost is similarly expressed as

$$R_S = \frac{R_{OP} + R_{PT} + R_{TP} + R_{PO}}{2}. \tag{2.9}$$

In the case of the first order ghost we have the two(**M1** and **M2**) on the same range, the only difference being the direction it goes.

$$R_{M1} = \frac{R_{OT} + R_{TP} + R_{PO}}{2} = R_{M2} \tag{2.10}$$

Identification and substitution in the denominator then yields

$$R_{M1} = R_{M2} = \frac{R_T + R_S}{2}, \tag{2.11}$$

stating that the first order ghosts are expected to lie halfway from target to second order in range. Taking the time derivative of this expression you get

$$D_{M1} = D_{M2} = \frac{\dot{R}_T + \dot{R}_S}{2} = \frac{D_T + D_S}{2}. \tag{2.12}$$

In other words, the first order is expected to be right in between the target and second order in Doppler as well. These two equations sums up to a linear relationship in range-Doppler like shown in figure 2.11. This relationship is what will be utilized to identify ghost reflections in this thesis.

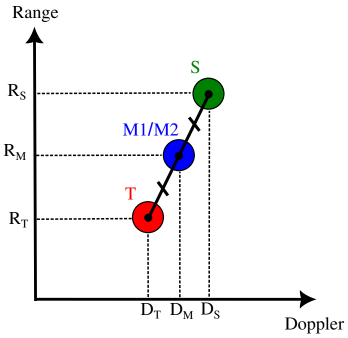

Figure 2.11: Linear relationship in range-Doppler between target(T), first order ghosts($M1/M2$) and second order ghost(S).

2.4 Hough Transform

In the previous section, a line on which the ghosts, along side the real target, should appear was described. Identifying lines in images can be done in different ways. The Hough transform is an example of an algorithm used for this. This is the approach used in this thesis. The Hough transform is widely used in computer vision and other forms of image analysis[17]. In the algorithm lines are expressed with two parameters, often named ρ(or r) and θ. ρ is the perpendicular distance from the line to the origin, while θ is the angle that line makes with the x axis, see figure 2.12. This way of expressing lines are superior to using k and m from $y = kx + m$, because vertical lines($x = n$) can easily be represented[18]. Usually when applying the Hough transform to an image, the edges occurring in that images is first retrieved. This because the edge lines are the ones of interest in most applications. There are many algorithms for retrieving the edges. However, in the context of this thesis, we are interested in finding lines among all detections, not just the edges. Detections are those points where the signal is over a certain threshold, and thereby considered to not originate from noise. For this reason we will simply regard all the detections as input to the transform.

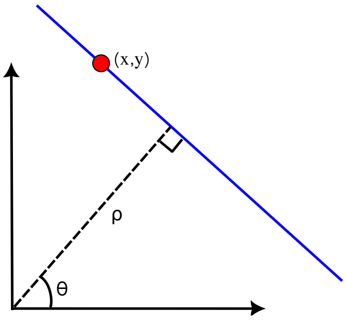

Figure 2.12: Hough representation of a line using the parameters ρ and θ.

The algorithm iterates through all the input points. For each point it draws lines with the corresponding ρ and a range of angles. Each of these lines gets a vote, stored in a voting matrix(often called Hough matrix). After the iteration is done lines with a high voting count represent the input well[18]. A simple illustration is seen in figure 2.13.

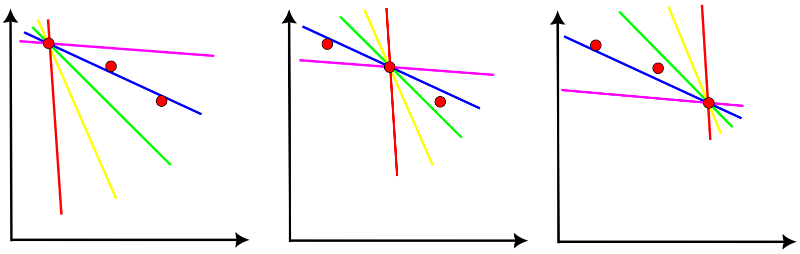

Figure 2.13: Example of an iteration over 3 points using the Hough transform. In this case the blue line estimate the points the best.

2.5 Clustering

Clustering is a central task when making sense of data. In the particular case of this thesis, the goal of the clustering is to separate detections in the range-Doppler domain, belonging to **T**, **M** and **S** respectively. Remember that these three clusters are expected to satisfy a linear relationship explained in section 2.3. There are a wide range of popular clustering algorithms. Some of which need the number of clusters as input, like K-means, and others that work independently of that, like DBScan[19]. In the next section the clustering method used in this thesis is presented.

2.5.1 Clustering Algorithm ABScan

When working with radar data, detections are usually gathered around high signal peaks. Detections are the signals that exceed a certain threshold, and hence are regarded as not just noise. Since the detections are centered around peaks, a reasonable way of approaching clustering is to form clusters around the peaks. This is the idea behind the algorithm ABScan (Amplitude-based spatial clustering of applications with noise). It is based on DBScan (Density-based spatial clustering of applications with noise)[20], which is a popular clustering method in various applications. However, as mentioned, ABScan uses the amplitude information, unlike DBScan. Two changes have been done to the DBScan algorithm. First of all, a pre-processing step has been added where all detections are sorted from highest to lowest SNR, where SNR is the signal-to-noise-ratio. The SNR says something about how strong a detection is compared to the noise floor. The second change has to do with the assignment of a cluster to a detection. The ABScan algorithm assigns a detection to the same cluster as its strongest neighbour, and the neighbours of a detection are defined by a distance function. Pseudocode for the algorithm is shown in Algorithm 1. A distance function needs to be chosen for the algorithm. This function should accept two points and return a measure of the distance between those points. The algorithm takes two parameters as input; the ϵ which is the largest distance at which two points are considered neighbours, and the ***minPoints*** parameter which sets a lower limit to the size of clusters.

Algorithm 1 ABSCAN

```
snr ← array of snr values
sortedIdxs ←sortDescending in SNR
labels ← array filled with -1
nextLabel ← 0
for p in sortedIdxs do
    largestNeighbourIdx ← p
    largestSnr ← snr[p]
    for other in sortedIdxs do
        if distance(p, other) > eps then
            continue
        end if
        if snr[other] > largestSnr then
            largestSnr ← snr[other]
            largestNeighbourIdx ← other
        end if
    end for
    if largestNeigbourIdx = p then
        {no neighbour with higher SNR, start new cluster}
        labels[p] ← nextLabel
        nextLabel ← nextLabel + 1
    else
        {neighbour with higher SNR, merge with that cluster(since neighbor had higher SNR
        it must have been processed and has an assigned cluster)}
        labels[p] ← labels[largestNeigbourIdx]
    end if
end for
for label in uniqueLabels(labels) do
    if count(label) < minPoints then
        labels[labels is label] ← -1
    end if
end for
return  labels
```

2.6 The Bistatic Problem

Estimating the angle of the first order signals, i.e. with one reflection in the reflecting surface, is challenging for a MIMO radar. These are the reflections named **M1** and **M2** in the multipath model in 2.2. A MIMO radar is what has been used in this thesis and the working principle is explained in section 2.1.3. The challenging angle estimation, sometimes referred to as the bistatic problem[21], was realized about halfway through the thesis process. Therefore this angle information has not been completely discarded, and a comparison to using the second order reflections **S** is included. These don't exhibit the bistatic problem. The comparison shows indication that discarding the information because of this problem is not motivated, at least in the scenarios investigated in this thesis. More on this in section 4.6, where the result of the comparison is presented.

The reason that the bistatic problem is only occurring for first order reflections(**M1** and **M2**) is that the direction-of-departure(DoD) and the direction-of-arrival(DoA) is not the same. Remembering the multipath model in section 2.2, we know that for first order reflections the DoD can be the target direction and the DoA the direction of the reflection, or vice versa. This difference in DoD and DoA introduces distortion of the channel phases[6], used to estimate the direction, as described in section 2.1.3. This is a distinct difference from the target **T** and the second order reflection **S**, both fulfilling DoD=DoA, and hence not affected by this phase distortion.

To what extent the phase distortion affects the angle estimation is varying in different cases. This has however not been in focus in this thesis. In figure 2.14 two simulations have been done just to illustrate how different the performance can be. The simulations are done under ideal conditions; there is no noise and the targets behave as point scatterers. Each subfigure contains simulation results of the angle estimation in three scenarios: a single target, two targets placed in θ_1 and θ_2, and a target in θ_1 along with a first order multipath detection with DoD $= \theta_1$ and DoA $= \theta_2$. Looking at subfigure (a) with $\theta_1 = 0°$ and $\theta_2 = -30°$, we can see that all three cases are well resolved. All three spectrums contain one or two peaks fairly well situated in 0ºand -30º. Looking at subfigure (b) on the other hand, where $\theta_1 = 0°$ and $\theta_2 = -50°$, the single and two target simulations produce good results while the spectrum for the first order multipath scenario is struggling. There are in the multipath spectrum(green) about six peaks of roughly the same size. This is due to the bistatic problem, originating in the discrepancy of DoD and DoA. We can by these simulations conclude that there are situations when the angular information of the **M**-ghost will be of very poor quality but also situations when the quality will be good. Determining in which situations the quality is good and in which it is poor is a topic for future investigation, and not in focus in this thesis. This is however an indication that the angular separation of target and **M**-ghost seems to affect the quality.

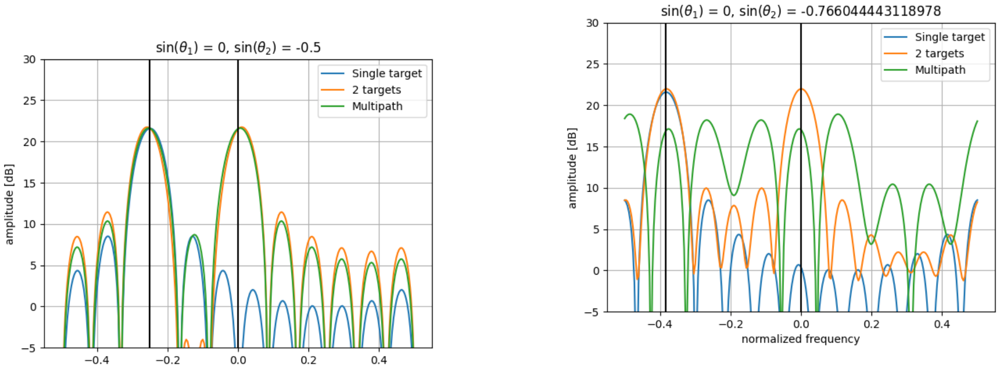

(a) $\theta_1 = 0°, \theta_2 = -30°$

(b) $\theta_1 = 0°, \theta_2 = -50°$

Figure 2.14: Figure shows simulations of angle estimation for three cases: a single target in θ_1 denoted by a blue line, two targets in positions θ_1 and θ_2 denoted by an orange line, and lastly a target in a scene such that a first order multipath occurs with angles θ_1 and θ_2 as DoD and DoA denoted by a green line. The two simulations are done with 30°of separation and 50°of separation. The two vertical black lines denote θ_1 and θ_2.

Chapter 3

Method

In the following chapter an algorithm will be presented which aims to estimate the position of a reflective surface which causes multipath detections. The algorithm implemented in this thesis does not use methods assuming a known geometry, such as ray tracing as used by the references presented in 1.3.1. In order to identify multipath signals it instead utilizes the mathematical relationship derived by Feng et al.[6], presented in section 2.3. Since the relationship is completely independent from any prior knowledge of the geometry of the scene, this means that contrary to ray tracing methods, no set up when installing the radar in a new location is required to use this algorithm.

Using this methodology the following tasks are performed in order to predict the position of the reflective surface which causes multipath detections:

- Identify target **T**, along with associated **M**-ghost and **S**-ghost.
- Use the range and azimuth angle information of **T** along with either **M** or **S**, to estimate the position of the wall.

The reader should know that most of the method was designed before we were aware of the existence of the bistatic problem, explained in section 2.6. This means that the algorithm was designed without the knowledge of the theoretically poor quality of the first order angle information, and hence said angle information is used. The results and consequences of this will therefore be presented and discussed in the thesis.

3.1 Overview of Implementation

A generalized version of the algorithm pipeline can be seen in figure 3.1, starting with input of raw data, recorded with the radar module, and ending up with wall predictions as output. The pipeline is divided into sections, with the first being processing of the raw radar data. This is followed by a multipath detection section, where detections are identified, clustered and tested for the **T/M/S** linear relationship, using a modified Hough transform. The proposed **T/M/S**-positions are then forwarded to the geometry section, where finally the wall estimations are produced using the range and angular information of each of these positions. All the steps in the pipeline will be discussed further in the following sections.

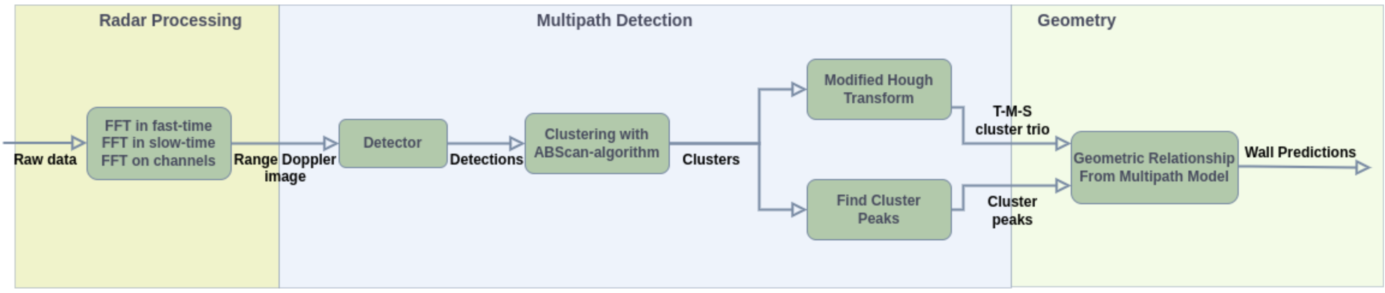

Figure 3.1: Pipeline of the wall estimation algorithm.

3.2 Raw Data Cube Processing

In this section the first part of the pipeline, called *Radar Processing* in Figure 3.1, is explained. The aim is to extract the three basic quantities of radar data; range, Doppler-speed and angle, from the raw radar data. Then this will be reduced to just range and Doppler which is the main domain of this thesis.

The three FFTs(range, Doppler, angle), explained in the *Theory* chapter, are applied to the data, resulting in a cube effectively composed out of a range-Doppler map for each virtual channel, i.e. TX/RX pair. It is in the range-Doppler domain the linear relationship for target **T** and the two category ghosts **M** and **S** is searched for. In order to shrink to just working with one range-Doppler map, the maximal signal amplitude out of the channels is chosen for each range-Doppler bin. In this range-Doppler map, the amplitude value for a bin with range R and Doppler speed D will be denoted by the function $A(R, D)$. It is in the range-Doppler image detections are found, which is the next step in the pipeline.

3.3 Detector

The detector performs the first operation in the *Multipath Detection* part of Figure 3.1. Its aim is to find the strong signals in order to keep working just with them. The detector takes the range-Doppler image and converts it into a binary mask of detections or activations. The mask contains 1:s and 0:s which correspond to range-Doppler bins which are classified as detections and non-detections, respectively. The bins which are classified as detections will then be forwarded to the subsequent steps in the algorithm, while the non-detections will in effect be ignored.

The detector that has been implemented is a simple variant of the order statistic constant false-alarm rate detector(OS CFAR)[22]. Detections are those range-Doppler bins with an amplitude $A(R, D)$ exceeding the noise floor with a threshold $\Gamma(R)$. The noise floor $N_f(R)$ was chosen as the median amplitude at the range R. In this thesis a simple threshold, partly varying with range was used. This threshold called $\Gamma(R)$ can be seen in figure 3.2. $\Gamma(R)$

was chosen in a rather manual manner, where this particular threshold was deemed to both generate clusters of appropriate size at close range and let through a minimal amount of noise at larger ranges while still catching weaker detections. The value of the detector $d(R, D)$ can be expressed as:

$$d(R, D) = \begin{cases} 1 & \text{if } A(R, D) > \Gamma(R) + N_f(R), \\ 0 & \text{otherwise.} \end{cases} \tag{3.1}$$

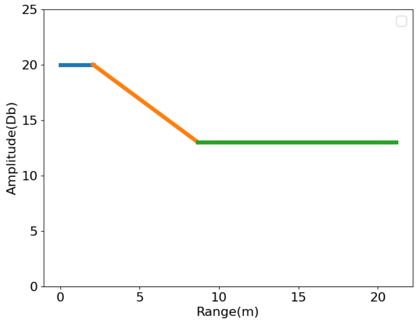

Figure 3.2: Detection threshold $\Gamma(R)$ plotted against the range R in m.

3.4 Clustering

In Figure 3.1 the subsequent step after the detector is the clustering of the detections. That is when we take the detections generated by the detector described above, and group them in clusters in the range-Doppler image. The goal of the clustering is to have clusters which correspond to logical parts of the multipath model. An ideal case would have a cluster each for the target, the first order ghost, and the second order ghost. This may not always be possible though, due to the assumption of the multipath model that the target is a point scatterer, which is not valid in real-life cases.

The clustering is done by the ABScan algorithm described in section 2.5.1. A weighted Euclidian distance was chosen as the distance function. For two points in the range-Doppler image with coordinates $p_1 = (R_1, D_1)$ and $p_2 = (R_2, D_2)$, the distance function $\delta(x_1, x_2)$ will be valued:

$$\delta(p_1, p_2) = \sqrt{(R_1 - R_2)^2 + \gamma \cdot (D_1 - D_2)^2} \tag{3.2}$$

The γ chosen was 0.5. This weight was chosen after observing that detections all belonging to the target were often divided into two clusters due to the large spread of the target detections in the Doppler dimension. A gamma lower than one allows clusters to extend further in the Doppler dimension compared to the range dimension, thereby counteracting the split into two. The ϵ was chosen to 3 which along with the chosen weight function and γ gave a cluster size which we considered adequate. The $minPoints$ parameter was chosen to 5, meaning that all detections belonging to clusters smaller than 5 detections were eliminated. This was chosen after some trial and error, and was deemed to perform well enough for our purposes. An extensive search for optimal clustering of radar data was not the focus of the thesis.

3.5 Choice of the range-Doppler Domain

The next section, *Modified Hough Transform*, begins to describe how the algorithm identifies detections which are multipath detections, and more specifically which detections are **M1/2** and which are **S**. Before we commence that argument we want to motivate why we have chosen to do the multipath classification in the range-Doppler domain instead of range-angle for example, range-angle meaning a 2D-domain with range on one axis and the angle of arrival on the other.

It may be possible to do the multipath classification in range-angle. One could there find detections and then look for detections or clusters which fulfill the geometrical relationship in figure 2.10. One advantage of working with Doppler-data instead of angle-data is that we do not have to consider the poor quality of the angular data for **M1** and **M2** due to the Bistatic problem (described in section 2.6) in the detection and clustering steps. For our algorithm, the poor quality does not have to be considered until we try to identify the multipath detections.

3.6 Modified Hough Transform

This section aims to discuss how our algorithm finds detections which lie in a straight line and according to the relationship in 2.3 could correspond to **T**, **M** and **S**. When looking back at figure 3.1, this is the box marked "Modified Hough Transform". It also discusses how this method differs from that of Feng et. al [6].

In the article by Feng et. al. [6] the Hough transform was suggested in order to find detections which lie in a straight line in the range-Doppler image. This in order to find three detections which could correspond to **T**, **M**, **S** as they should be situated on a straight line, with equal distances **T**-**M** and **M**-**S**, according to section 2.3. In the article by Feng they use the Hough algorithm with this purpose.

The Hough transform described in section 2.4 finds lines by letting each detection vote once on each line. The approach in the article by Feng et. al. was to then use lines which had three votes, one vote each for the target, first order and the second order. We found that this approach was unfit on real radar data for several reasons. Firstly, the number of votes that the lines with the most votes ended up with was often more than fifty. That induces the problem: What is the threshold marking the minimum number of votes for a line to be included? To set a constant threshold would be very difficult when the number of votes can change dramatically from frame to frame. This threshold may also change when the range to the target changes. Looking at subfigure (a) in figure 3.3 we can see two lines with lengths 37 and 33. Having a threshold of 3 would serve little purpose when lines receive a much higher number of votes. Secondly, the Hough transform did not seem to be favoring the lines which traversed the most clusters but rather the lines with the most votes were often just crossing one or a few very wide clusters. This is illustrated in figure 3.3 subfigure (a) by a comparison of the blue and the red line. The red line is preferable for our purposes, since it crosses three clusters which could correspond to **T**, **M**, and **S**. Looking at the votes though, we see that the red line has 33 while the blue has 37.

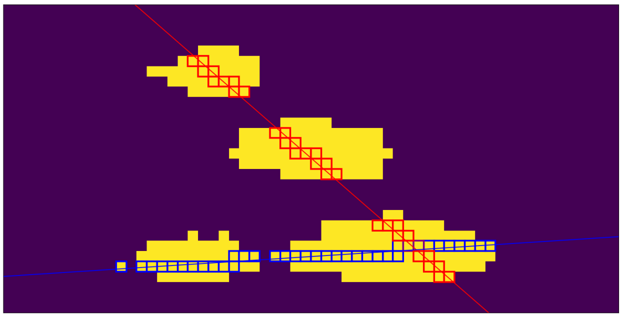

(a) Unmodified.

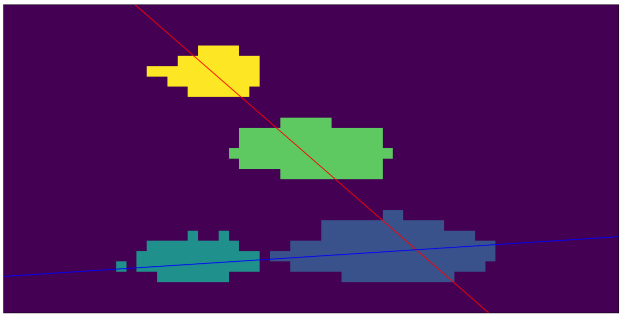

(b) Modified.

Figure 3.3: Subfigure (a) illustrates the unmodified Hough transform. Two lines, a blue and a red, are plotted along with their respective voting detections. The detections which voted for the blue line are framed with blue, while detections voting for the red line are framed with red. Purple framed detections voted for both. In total 37 detections voted for the blue line, while 33 voted for the red line. Subfigure (b) illustrates the same two lines but for the modified Hough transform where the clusters now vote instead of the detections. In this case the blue line gets 2 votes while the red line gets 3.

Instead of sticking to the transform described above, we chose a different route than done by Feng et. al., and we opted for a modified Hough transform where each cluster could only vote once per line. This change seemed both true to the purpose of the Hough transform, as well as a reasonable solution to the problems listed above. Returning to figure 3.3 but looking at subfigure (b) instead we can see that the red line receives three votes with this change to the Hough transform, while the blue only gets two.

With this algorithm change, the threshold for which a line is included in the next step is three clusters. Every line which passes through three or more clusters may potentially spawn a wall estimate.

3.7 Requirements to Spawn Wall Estimate

Previously the algorithm has dealt mostly with clusters and lines, but from here on it will be the cluster peaks, i.e. the largest value in each cluster, that will be used. In the section to come, these cluster peaks will be representative for the target **T**, **M**-ghost and the **S**-ghost. They are representative in the sense that the target position will be completely determined by the range and angle of the cluster peak of the **T**-cluster, and the same goes for the **M**-ghosts and the **S**-ghost. That the peak is a good representation for the entire cluster is an assumption that is not obviously true, but reasonable considering the peak of the cluster has the most energy. Upon evaluation of the results the assumption was deemed satisfactory.

The next step of the algorithm takes in a set of lines of which each passes through a minimum of three clusters. For a selection of three clusters to be classified as **T**-**M**-**S** and spawn a wall estimate there is a set of necessary conditions on the cluster peaks, shortly explained. The three cluster peaks will in the following account of these conditions be referred to as peak **T**, peak **M**, and peak **S**.

As previously stated, when designing this part of the algorithm we had no knowledge of the bistatic problem. The reader should therefore be aware that the angular information of the first order ghost was used without restraint when constructing the algorithm and some portions of the design might seem illogical knowing of the problem. The results and consequences of this will later be discussed. We can also conclude that the usage of the angular information is another significant distinction between this algorithm and the proposed solution by Feng et. al. [6].

3.7.1 Extracting Angular Information

The requirements on the three clusters use the extracted angular information of the cluster peaks. Recalling section 2.2, we remember that the target and the second order cluster have the same DoD as DoA, while the first order ghosts will differ in DoD and DoA. In figure 2.10 it is also clear that the DoA of **M1** coincides with the DoD and DoA of **S**, while the DoA of **M2** coincides with the DoD and DoA of **T**. From section 2.3 we know that the first order ghosts **M1** and **M2** have the same range and the same Doppler speed, meaning that these ghosts theoretically should overlap in the range-Doppler image. This reasoning leads us to believe that when looking at peak **T** and peak **S** we should see one dominant peak in their angular spectrums while it should be two in the overlapping **M1**/**M2** spectrum. Looking at figure 3.4 we see a typical example of angular spectrums for a **T**, **M** and **S** combination. In subfigure (a) and (c) we see one dominant peak while in subfigure (b) there are two, one with the same angle as **T** and one with the same angle as **S**. This appears to agree with what the theory suggests.

The process of extracting the angular information is done using the algorithm below. The vector produced by the angular FFT will be referred to as the angular spectrum, and a cluster which is tried as the target cluster will be referred to as the suspected target.

1. For the angular spectrum $\Omega_T(\theta)$ of the suspected target: Choose angle with the largest value of the spectrum, θ_1^T.
2. For the angular spectrum $\Omega_M(\theta)$ of the suspected first order: Choose angle with the

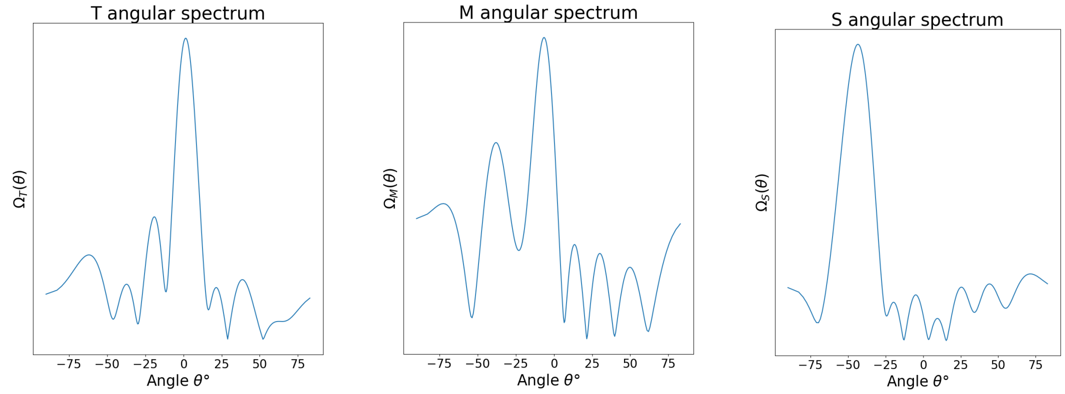

(a) **(b)** **(c)**

Figure 3.4: Angular spectrums from a frame which yielded good results for the peak of the T-cluster, M-cluster and the S-cluster.

largest value θ_1^M if it is not within $\pm\Delta_A$ angle bins of the suspected target's angle. If it is, the angle with the second largest peak θ_2^M is used.

3. For the angular spectrum $\Omega_S(\theta)$ of the suspected second order: Choose angle with the largest value of the spectrum, θ_1^S.

The reason for not choosing simply the angle bin with the largest value for the suspected first order, is that we desire to find the DoA for **M1** and **S** (i.e. angle of reflection), not **T** and **M2**. The Δ_A was in our thesis set to 2 angle bins. Why we chose to work with angle bins instead of degrees is simply that we started out with bins and found something that worked for our purposes. We then considered switching to degrees, but realized that when transforming from angle bins to degrees, the bins are smaller in the boresight of the radar while they are larger in the ends of the spectrum. A change to a static number of degrees would change the behaviour of the algorithm so we chose to keep it.

3.7.2 Necessary Conditions

With the angular information retrieved like this, the following conditions were enforced:

- The range of peak **T** must be at most Δ_R range bins away from the range of the nearest cluster peak among all clusters.

- The range of peak **M** minus the range of peak **T**, should be in between α_l and α_u of the range of peak **S** minus the range of peak **T**.

- The angular composition of peak **M** should contain two peak angles, which here means that the largest peak $\Omega_M(\theta_1^M)$, should at max be twice the size of the next largest peak in the angular spectrum $\Omega_M(\theta_2^M)$. In subfigure (a) of figure 3.5 the second largest peak should be above the red dotted line.

- The angular composition of peak **S** should only contain one peak angle, which here means that the largest peak $\Omega_S(\theta_1^S)$, should at least be twice the size of the next largest peak in the angular spectrum $\Omega_S(\theta_2^S)$. In subfigure (b) of figure 3.5 the second largest peak should be below the red dotted line.

Δ_R was chosen to 2 range bins, α_l to 1/3, and α_u to 2/3. These conditions are reformulated as an equation system in 3.3. Let us call the range of the nearest cluster r_{near}, the range of target peak r_T, range of first order peak r_M, and the range of second order peak r_S.

$$\begin{cases} r_T \leq r_{near} + \Delta_R \\ \alpha_l \cdot (r_S - r_T) < r_M - r_T < \alpha_u \cdot (r_S - r_T) \\ \Omega_M(\theta_1^M) < 2 \cdot \Omega_M(\theta_2^M) \\ \Omega_M(\theta_1^S) > 2 \cdot \Omega_M(\theta_2^S) \end{cases} \tag{3.3}$$

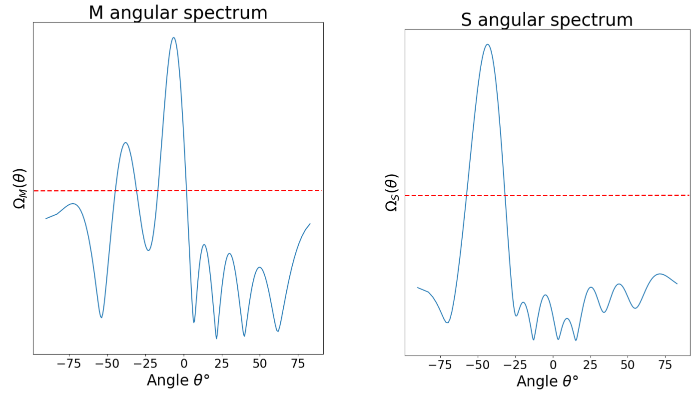

(a) **(b)**

Figure 3.5: Two angular spectrums for a first order ghost and a second order ghost. The dashed red line marks half the amplitude of the largest peak of the spectrum.

These conditions are there in order to discard combinations of clusters which lay in a straight line due to chance and not due to being a **T**-cluster, **M**-cluster and **S**-cluster. We began constructing these conditions upon seeing that the results without filtering the estimations rendered fairly rough results. The second condition was the first to be implemented, and it stems from the fact that theoretically peak **M** should be right in between peak **T** and peak **S** in the range-Doppler image. The limits $\alpha_l = 1/3$ and $\alpha_u = 2/3$ were found to eliminate the very faulty suggestions of **T**, **M** and **S**, but also not exclude correct **T**, **M** and **S** combinations which due to discrepancy between theory and real data do not perfectly fulfill equations 2.11 and 2.12. Subsequently, the first condition was constructed when observing selections of three clusters where the nearest cluster was not actually part of the target. Lastly, the third and fourth conditions were added in order to filter out cluster combinations where the ghosts do not look like what we expect, discussed in section 3.7.1. This addition was observed to even further improve the accuracy and remove outliers.

3.8 Geometry Calculation

The algorithm now enters the geometry block, pictured in figure 3.1 as the rightmost block. This is the final step where the range and angle information of the target and the second (or first) order ghost gets converted into an estimate of the wall position. The process of doing this is quite simple but slightly different for the **S**-ghost versus the **M1**-ghost.

3.8.1 Second Order Geometry Calculation

When it comes to the second order ghost, the process of estimating the wall position is done solely using linear algebra. In figure 3.6 the geometric characteristics of a second order multipath ghost is drawn. From the figure we realize that the second order ghost is the reflection of the target in the wall segment. Knowing that and the positions of the target $\mathbf{p}_T$ and the **S**-ghost $\mathbf{p}_S$, the wall segment can be calculated in the following way:

1. The wall segment must be on the line marked with a gray dashed line in figure 3.6. The midpoint in between **T** and **S**, $\mathbf{p}_T + 0.5 \cdot (\mathbf{p}_S - \mathbf{p}_T) = 0.5 \cdot (\mathbf{p}_S + \mathbf{p}_T)$, is on this line and the wall normal vector $\mathbf{n_w}$ can be calculated by normalizing $\mathbf{p}_S - \mathbf{p}_T$. From $\mathbf{n_w}$ we can calculate $\mathbf{e_w}$.

2. We can also conclude that the wall segment should be situated on the line which passes through the radar in the origin and the second order ghost $\mathbf{p}_S$. This is in the direction $\mathbf{e_S}$.

3. The position of the wall segment is found by calculating the intersection of these two lines.

3.8.2 First Order Geometry Calculation

Using the first order ghosts to make a wall estimate is in this thesis not as common as using the second order ghosts. As talked about in section 2.6 the angle information of the first order ghosts is not as reliable as the second order ghosts due to the inherent property that DoD $\neq$ DoA. The first order estimate was used and compared to the second order estimate in section 4.6.

In figure 3.7 the geometry of a first order ghost is displayed. From the multipath model detailed in section 2.2 we know that the total path length of the first order ghost is $r_T + k_2 + k_1$. Knowing the range and angle of the **M**-ghost, a simple optimization along the line from the radar to the first order ghost can retrieve the wall position. A bisection optimization algorithm [23] with the objective function $f : f(k_1) = k_1 + k_2(k_1) + r_T - 2 \cdot r_M$ and start values $k_1 = 0$ and $k_1 = r_M$ was implemented. $k_2(k_1)$ signifies the function that is valued to the length of k_2 given that the reflective wall segment is situated a length k_1 from the radar, in the direction of $\mathbf{e_M}$. The start values correspond to the endpoints where the reflective wall segment is placed in the radar position ($k_1 = 0$), or the **M**-ghost position ($k_1 = r_M$). The objective function is valued to zero when $\frac{k_1+k_2(k_1)+r_T}{2} = r_M$. This is the same as equation 2.10 with $r_T = R_{OT}$, $k_1 = R_{PO}$ and $k_2 = R_{TP}$, meaning that the optimization will if successfully completed yield the correct **M1**-position.

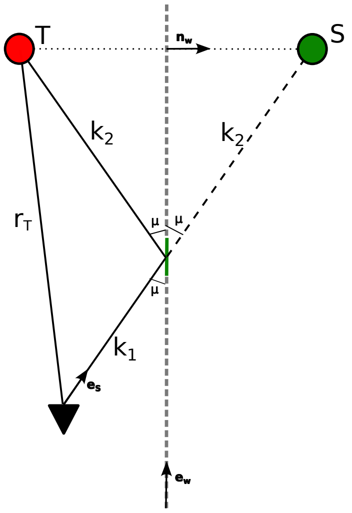

Figure 3.6: Second order geometry. The black triangle is the radar. The red and green circles are the target and the second order ghost. The wall segment responsible for reflecting the signal is in green, and the segment is extended with the gray dashed line. r_T is the range of the target while k_1 and k_2 are the lengths of the path that the second order signal takes, before and after the two wall reflections. $\mathbf{e_w}$ is the wall unit vector, $\mathbf{n_w}$ is the wall's normal vector and $\mathbf{e_S}$ is the second order unit vector.

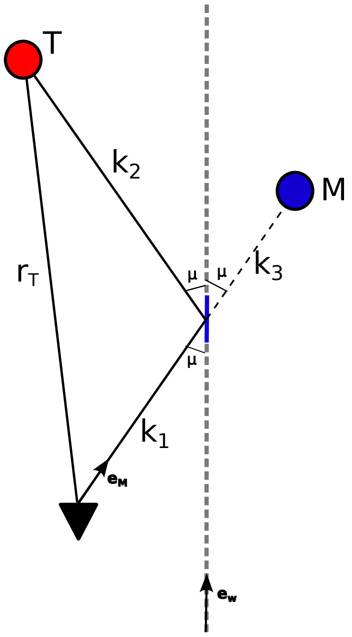

Figure 3.7: First order geometry. The black triangle is the radar. The red and blue circles are the target and the first order ghost. The wall segment responsible for reflecting the signal is in blue, and the segment is extended with the gray dashed line. r_T is the range of the target while k_1 and k_2 are the lengths of the path that the first order signal takes, before and after the wall reflection. $\mathbf{e_w}$ is the wall unit vector and $\mathbf{e_S}$ is the second order unit vector.

3.9 Radar Specification and Mounting

Data was collected with a commercially available FMCW radar system, mounted at a height of 1.40 m, with boresight being parallel to the ground. This height was chosen due to it being roughly chest height of the targets, thereby making the area in the radar plane as large as possible. The FMCW radar parameters are presented in table 3.1. Worth to note is that a bandwidth of 3 GHz is categorized as ultra-wideband. This was chosen because increased range resolution was deemed needed for the algorithm.

Parameter	**Value**
Center Frequency	60 GHz
Bandwidth	3 GHz
No. Tx	2
No. Rx	4
Chirp Time	33.850 μ s
Frame Time	25.000 ms
Max Range	21.141 m
Range resolution	0.041291 m
Max Doppler	9.864 m/s
Doppler resolution	0.01927 m/s

Table 3.1: Specification for the radar used in the thesis.

3.10 Setups

In order to investigate how well our algorithm performed a couple of different setups were used. The recordings were made in a gym of approximate size 30x15 meters. The location was chosen because it was a controlled environment, where potentially disturbing objects could be moved out of the way. In order to simulate an environment with strong multipath reflections, relevant portions of the wall of the gym was covered with a 0.43m wide strip of aluminium foil, centered at a height of 1.35m. Radar signals reflect well off metallic surfaces[24]. The results later presented will all, with one exception, be using aluminium foil. It is important to note that this is not a facilitating measure that lessens the importance of the results, but rather a way for us to ensure that multipath reflections will occur, like they do in many real-world applications where aluminium foil is not used.

Down below the setups defining radar position and orientation in relation to the walls are listed. The camera pictures show the radar mounted on its stand, along with the walls covered in aluminium foil.

3.10.1 Single Parallel Wall

The setup we call *Single parallel wall*, is with the radar aligned along the wall, with a displacement of 1.25m between them. In the recording the target is simply walking along boresight of the radar. The wall is covered with aluminium foil. This makes it so that the signal can reflect off the foil even when the target is furthest away from the radar along the wall. See the setup in figure 3.8. The aim of setting the scene up like this was in order to investigate the absolute simplest case first. This is the simplest case since there is just one wall and it was hypothesized that it is simpler with a wall parallel to the boresight than a perpendicular wall.

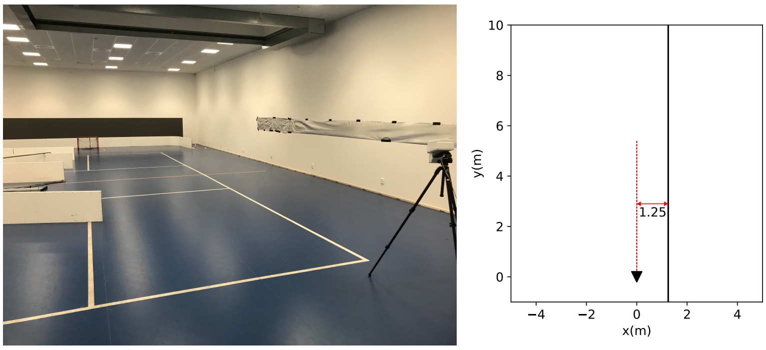

Figure 3.8: The *Single parallell wall* setup. Boresight of radar along the wall, which is displaced 1.25m from the radar.

3.10.2 Varying Wall Angle

The aim of this setup was to investigate how the angle between boresight and wall affected the algorithm performance. Naturally a radar is faced with all kinds of reflectors, with different angles, based on where it is mounted. Therefore expanding the *Single parallell wall* setup to different relative angles to the wall was of interest. The setups can be seen in figure 3.9. An important disclaimer is that the amount of occlusion in the different setups was not taken into account when the recordings were performed. In some of the recordings the target basically never occluded the signal from reaching the wall, whereas in others the wall was occluded in a significant part of the recording. Therefore it is not valid to draw big conclusions from the impact of the angle of the wall, since it is not the only parameter varied. Another investigation solely varying angle would be needed for stronger conclusions to be drawn. The time frame of the thesis made this unfeasible however.

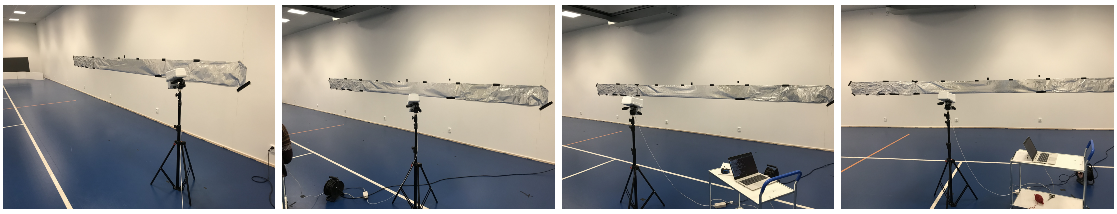

(a) 22.5°

(b) 45°

(c) 67.5°

(d) 90°

Figure 3.9: Setup with varying angle relative to the wall.

3.10.3 Aluminium vs. No Aluminium

It was of interest to compare how much the aluminium foil amplified the multipath effects and thereby affected our results. Therefore one setup was used where one recording of each was made, with and without aluminium. The setup with the foil up can be seen in figure 3.10. The wall was aligned along boresight of the radar with a displacement of approximately 1.23m and the target is simply walking along boresight.

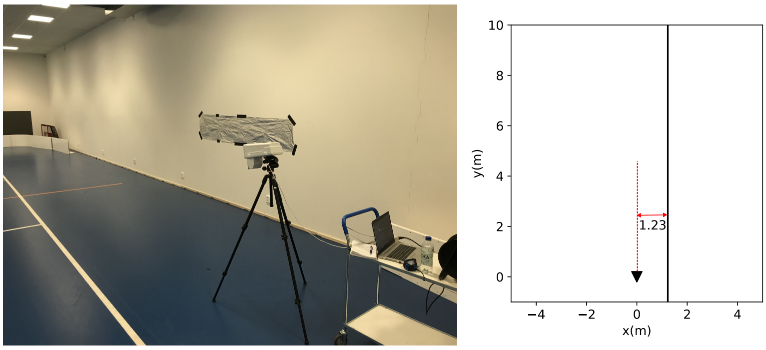

Figure 3.10: Setup used when comparing aluminium on wall versus not, showing the aluminium version. Boresight of radar is aligned with the wall and the distance between them is 1.23m.

3.10.4 Tunnel

This setup was constructed with a second "wall"(using screens) at the same distance from the target, walking along boresight. Sheets of aluminium foil were attached to both the wall and the screens. What makes this setup interesting is that the reflections off each wall will have the same range and Doppler, only varying angle. This makes it a very challenging case, if not impossible for our algorithm. At least if you want to get estimations for both walls at the same time in a single frame. The algorithm hasn't been implemented to expect more than two angles of interest per range-Doppler bin, the target angle and the wall angle. So in this setup two wall angles can be present in a range-Doppler bin, in addition to the target angle. Therefore we thought of this as an interesting test. The setup is visualized in figure 3.11.

3.10.5 The L

With the screens used in the "Tunnel" setup, an L shaped wall was also used. This would be similar to how the algorithm would handle a corner. Aluminium foil was attached to the screens as well as the wall. The radar was setup with an angle to the wall this time. This with the intent to facilitate for the signal to reflect off the screens, compared to having the radar along the wall and the screens perpendicular to the radar. The setup is explained visually in figure 3.12.

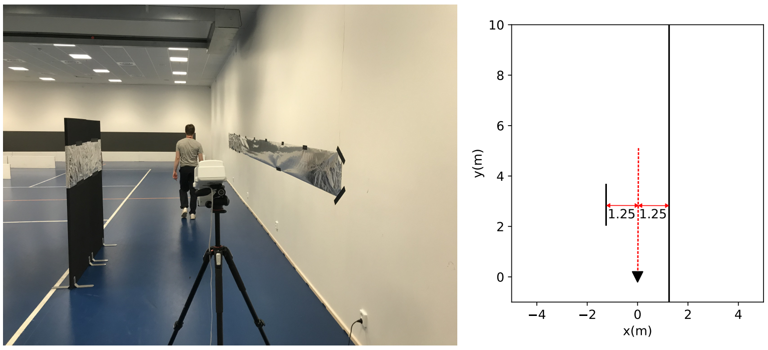

Figure 3.11: The tunnel setup with a screen placed at equal distance from the radar's boresight as the wall.

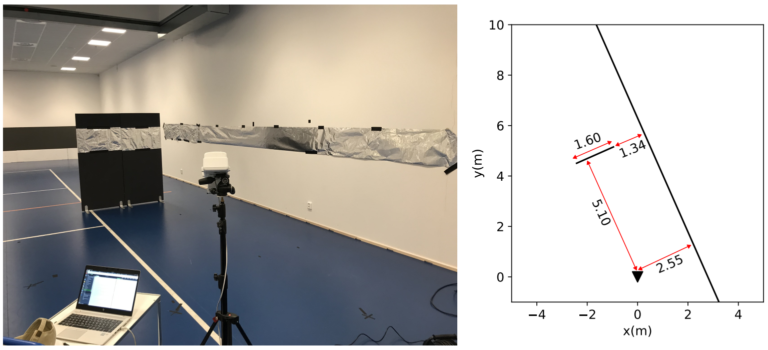

Figure 3.12: The L setup.

Chapter 4

Results & Discussion

The results from the different setups explained in the *Setups* section(3.10) are presented and discussed below. For all setups the recording is divided into either 2, 3 or 4 segments. This is done in order to facilitate the interpretation of the results; by simply uncluttering the wall estimations and by being able to separately analyze different parts of the recording.

During the process of the thesis, a realization that the second order ghosts theoretically should produce much better wall estimates due to the bistatic problem, was reached. Therefore the bulk of the result is of these second order estimations. However it is of interest to compare these to using the information in the first order ghosts instead. This is done in section 4.6. The chapter is concluded with discussing possible future work.

4.1 Single Parallel Wall

The *Single parallel wall* setup is the simplest variant with only one reflective surface present in the field of view, angled completely parallel with the direction of the radar. Figure 4.2 displays the second order wall estimates for four separate segments of the recording. The movement of the target in each of these segments is shown in figure 4.1. Subfigures (a)-(d) of figure 4.2 contain the results for each of these segments; the green circles being the second order wall estimations, the red and green crosses being the target and second order ghost positions identified by the algorithm. The only targets that are plotted are those which actually yielded wall estimates. In other words, the target has been identified in more frames, but only plotted for the frames where **T**/**M**/**S**-lines, resulting in wall estimates, has been found. Subfigure (e) contains the results of all sections aggregated, but plotted without identified targets and **S**-ghosts. Subfigure (f) contains the cumulative distribution of the errors of these wall estimations. The cumulative distribution depicts the proportion of estimate errors that are smaller than the error on the x-axis.

First off, an observation can be made that the **S**-positions, marked by green crosses in subfigures (a)-(d), show up as the **T**-position mirrored in the wall most of the time. This is

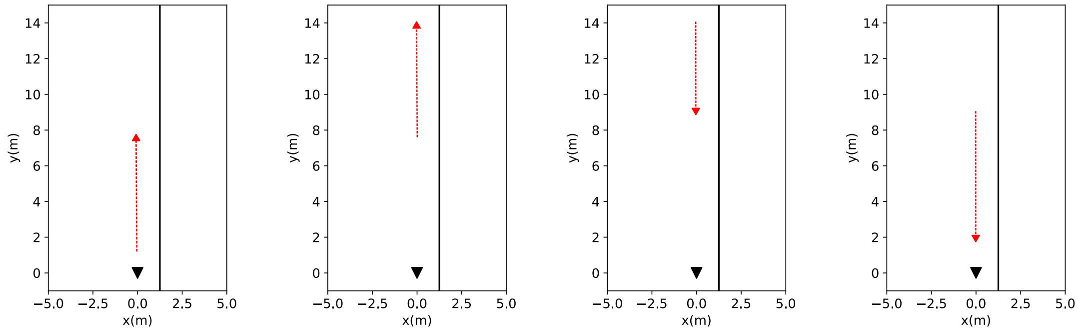

(a) (b) (c) (d)

Figure 4.1: Movement of the target in the sections presented with wall estimates in figure 4.2. The wall is marked with a black line

what we expected from the multipath geometry, and shows that the selection of **S**-clusters in the range-Doppler map is working well. Subfigures (a) and (d) of figure 4.2 contain a significantly higher number of wall estimates compared to subfigures (b) and (c). Figure 4.1 shows that (a) and (d) correspond to the segments of the data set where the target is closer to the radar, while in (b) and (c) the target is further away. There are several reasons as to why a target that is further from the radar yields fewer wall estimates:

- The signal energy decreases with the range r as $\frac{1}{r^4}$ in theory, making it harder to detect target, **M**-ghost and **S**-ghost [25].
- When the target moves further from the radar in this data set, the position of **T**, **M** and **S** approach each other in the range-Doppler image. This because the length of the path reflecting in the wall more and more approaches the length of the direct path to the target.
- As the target moves away, the angular separation of **M1** and **M2** diminishes, due to that the direction of reflection in the wall approaches the direction of the target. This effect makes it more difficult to classify the **M**-cluster as such. The algorithm is expecting more than one prominent peak in the angle spectrum Ω_M, and the **M1**- and **M2**-peaks approach each other and merge into one peak, resulting in the algorithm discarding the **T/M/S** combination.

We can also note that subfigure (b) and (c) look quite different with a few wall estimations at a range of around 8 meters for (b), while subfigure (c) has a few wall estimations when the target is at 10-14 meters of range. The main difference between these segments is that the target walks away from the radar in (b) while it walks towards the radar in (c). Another unfortunate difference is that the segments are of unequal size; (b) ranges from 8-14 while (c) from 14-9. This slight difference is what causes more estimates to appear around the 8 meter range for (b). Why there are four wall estimates on the target range of 10-12 meters in (c) while there are no estimates in (b) is hard to answer. It could have something to do with whether the target is walking away or towards the radar.

From subfigure (f) of figure 4.2, showing the cumulative distribution of wall estimate errors, we can retrieve that the median error, i.e. the 50th percentile, is 8 cm. In other words half of the estimates are closer than 8 cm to the correct wall, indicating that the algorithm is

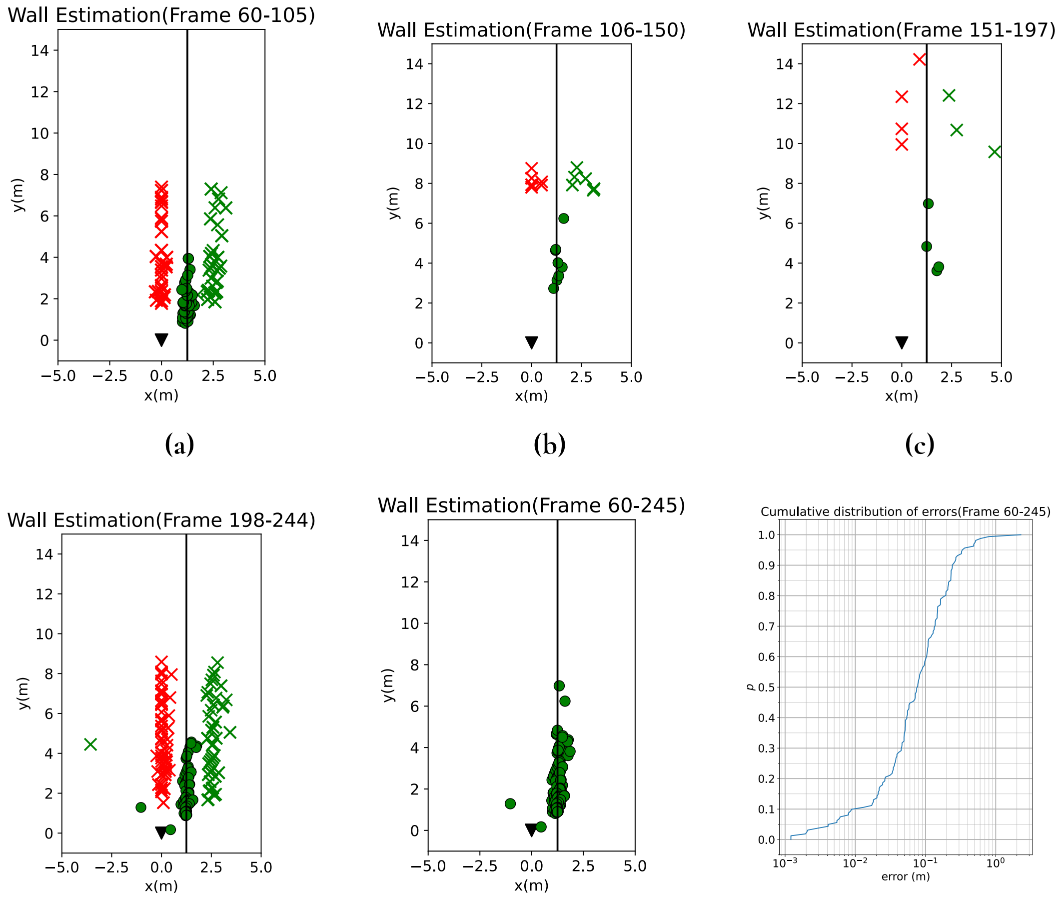

(a) (b) (c)

(d) (e) (f)

Figure 4.2: The red and green crosses are the targets and second order ghosts respectively, which contributed with a wall estimate. The green dots are the produced wall estimates. The black line is the wall. The black triangle is the radar position, pointing in the y-direction. (a)-(d) contains the sections with target movements described in figure 4.1, while (d) is the sum from all the sections with just the estimates. (f) shows the cumulative distribution of the errors of the wall estimates.

performing pretty well. The 90th percentile was 24 cm. An accuracy of 24 cm or better for 90% of the estimates is another argument for that the algorithm works well, at least with this particular geometry and target path.

Quantifying the precision of the wall estimates is easy since the position of the wall relative to the radar is measured when setting up the radar. Another quantitative measure of how well the algorithm performs would be the precision of the T, M, and S classification. This would be significantly harder to produce since there is no ground-truth to what clusters are **T**, which are **M** and which are **S**. This is real data so one could try to manually annotate it, but even then it is not completely clear to someone who has worked for a long time with this what is **T**, **M** and **S**. It is therefore hard to produce accurate results on the precision of the classification. An indication on how well the algorithm classifies **T**, **M** and **S** can be drawn from the wall estimation precision, since this estimation relies heavily on that clusters are labeled correctly. Continuously good wall estimations can be considered an indication of mostly correct classification.

In figures 4.3, 4.4 and 4.5 the results for single frames are presented. This as a representation of what the performance of the algorithm can look like in single frames. There are four subfigures in 4.3 and 4.4. Subfigure (a) contains the wall estimations generated from the frame. Subfigure (b) contains the camera image. Subfigure (c) contains the detections clustered with the ABScan algorithm, each color representing a cluster. The purple color is non-detections. Subfigure (d) contains the same clustered detections, along with lines found by the modified Hough transform. In figure 4.5 the algorithm has failed to find any lines which fulfill the conditions in section 3.7.2, which is why this figure only contains subfigures (a)-(c).

Starting with figure 4.3, the target can be seen at a range of approximately 3 m. Subfigure (a) contains one wall estimation, in the form of an **M**- and **T**-estimation, indicated by a blue and green circle respectively. Subfigure (c) and (d) indicate that the detections were clustered in 4 clusters. The clustering of the detections visible in subfigure (c) are familiar, keeping in mind that we are searching after the **T**/**M**/**S**-lines with similar distances for **T**→**M** and **M**→**S**. There are three large clusters which are situated in a fairly straight line; the center cluster marking the midway point of the outer clusters. These could be the target, **M**-ghost and **S**-ghost, in order of smallest to largest range. The cluster peaks are the rd-bins that the algorithm uses to estimate the wall positions. The performance of the algorithm heavily depends on our hypothesis that these bins are satisfactory representatives of the target, **M**-ghost and **S**-ghost. These points, which are marked by a black cross in subfigure (c), appear to follow the theory from subsection 2.2 fairly well in this frame. They are not situated in a perfectly straight line but nearly. There is a fourth cluster which is small and on the same range as the target. This is likely a part of the target which moves slower than the rest, like an arm or a leg. Figure 4.4 displays the result of another frame. The clustered detections are here divided into 7 clusters. The target and first order seem to have been divided into two clusters each; a slower and a faster cluster. There are two potential candidates for the second order cluster. This jumble of clusters produces four estimates each of **M**- and **S**-ghosts. The estimations have a slight spread in both x and y direction, while being mostly centered around the real wall. The fact that the estimates even when noisy, retain some level of sturdiness, is promising for the overall result of the algorithm.

Lastly, figure 4.5 contains a frame in which no Hough lines passed the requirements in subsection 3.7.2 to produce a wall estimate. The clustered detections in subfigure (c) has

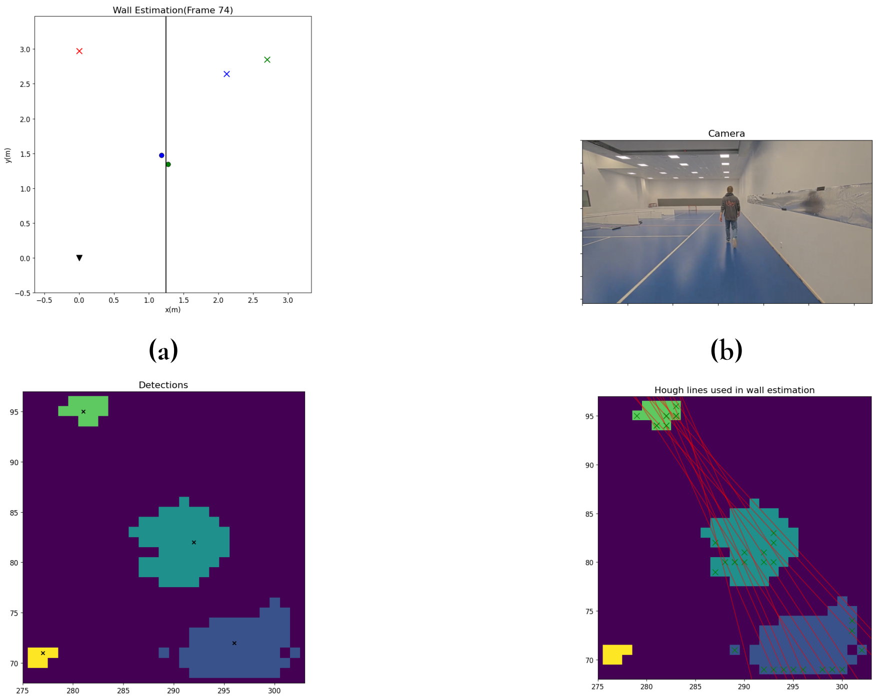

(a) (b)

(c) (d)

Figure 4.3: Figure contains the results of frame 74. Subfigure (a) contains the wall as a black line and the radar-location signified by a black triangle. The target-locations along with the first order ghosts and second order ghosts are denoted as red crosses, blue crosses and green crosses, respectively. The first order wall estimates are denoted by blue circles while second order wall estimates are denoted by green circles. Subfigure (b) contains the camera picture from frame 74. Subfigure (c) depicts the clustered detections where non-detections are colored dark-purple and each cluster has its own color. The black crosses mark the largest value of each cluster. Subfigure (d) contains the Hough lines that were used to spawn wall estimates, projected on top of the clustered detections.

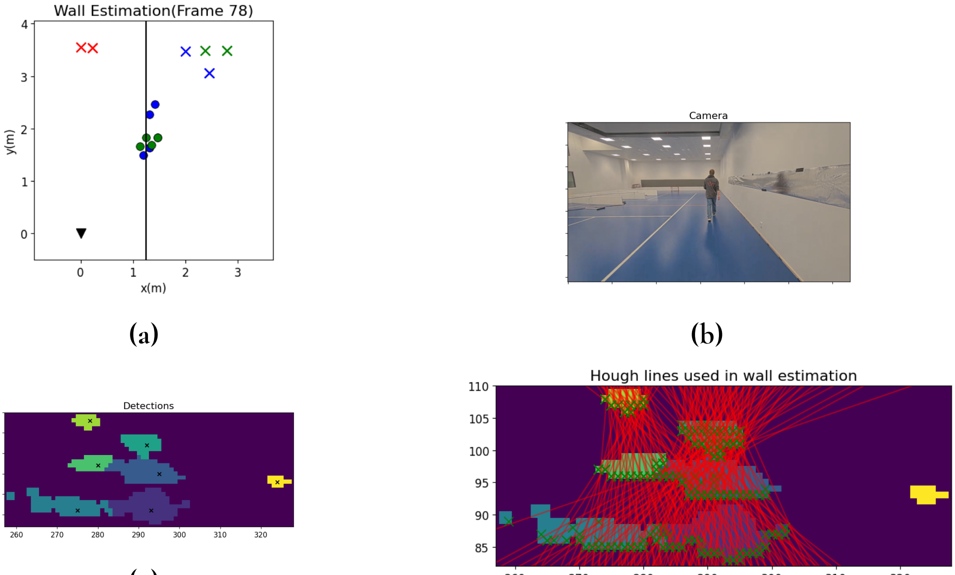

(a)

(b)

(c)

Figure 4.4: Figure contains the results of frame 78. Subfigure (a) contains the wall as a black line and the radar-location signified by a black triangle. The target-locations along with the first order ghosts and second order ghosts are denoted as red crosses, blue crosses and green crosses, respectively. The first order wall estimates are denoted by blue circles while second order wall estimates are denoted by green circles. Subfigure (b) contains the camera picture from frame 78. Subfigure (c) depicts the clustered detections where non-detections are colored dark-purple and each cluster has its own color. The black crosses mark the largest value of each cluster. Subfigure (d) contains the Hough lines that were used to spawn wall estimates, projected on top of the clustered detections.

three clusters in a line which could correspond to the **T**, **M**, and **S**, but due to the angular compositions of the cluster peaks, no estimate has been produced. As a comparison, a manual selection of **T/M/S** candidates, fed to the algorithm was done. Figure 4.6 shows the results of this. Subfigure (a) displays the range-Doppler image with the three cluster peaks manually selected marked with small circles. Subfigure (b) shows the wall estimation, with green dot for the estimation and red/green crosses for target/ghost positions. It indicates that the frame result could be very accurate. The estimation has an error of a few centimeters. Frames such as this one occur and demonstrate that there is room for improvement concerning the method of discarding cluster trios presented in section 3.7.2. This cluster trio is discarded due to the angular spectrum of the supposed **M**-cluster peak. That spectrum is presented in subfigure (c). According to the conditions in section 3.7.2 the spectrum of the **M**-cluster should have two peaks where the smaller of the two must be at least half the amplitude of the larger. As can be seen in subfigure (c) the next largest peak is not half as big as the largest. A further improvement to the algorithm could be to use more of the information in the supposed **M**-cluster, instead of just using the spectrum of the cluster peak. For example searching a specified area around the peak bin, and only discarding if none of the bins contain angle spectra satisfying the condition. This may improve the accuracy of which cluster trios are discarded.

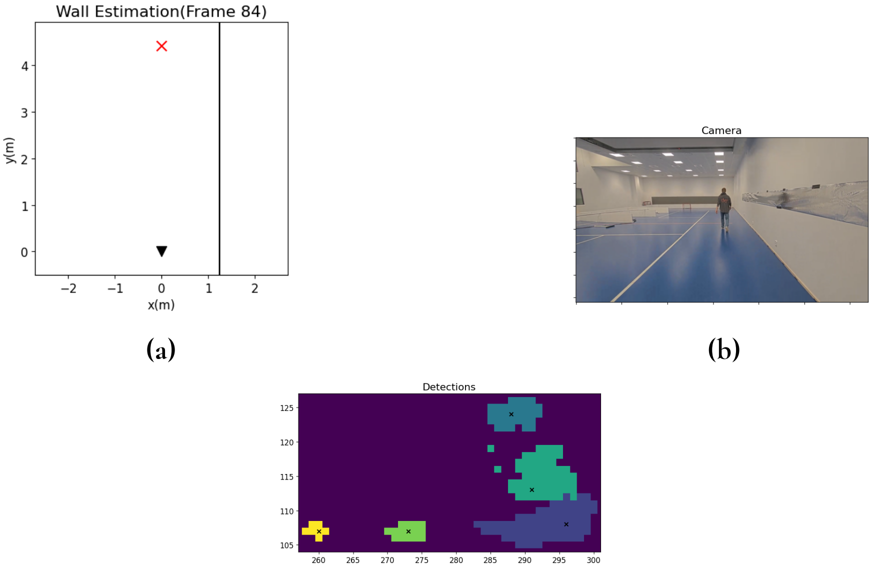

(a) **(b)**

(c)

Figure 4.5: Figure contains the results of frame 84. Subfigure (a) contains the target-location as a red cross, the wall as a black line and the radar-location signified by a black triangle. There are no wall estimates in this picture and the target is therefore chosen as the peak of the closest cluster in range. Subfigure (b) contains the camera picture from frame 84. Subfigure (c) depicts the clustered detections where non-detections are colored dark-purple and each cluster has its own color. The black crosses mark the largest value of each cluster.

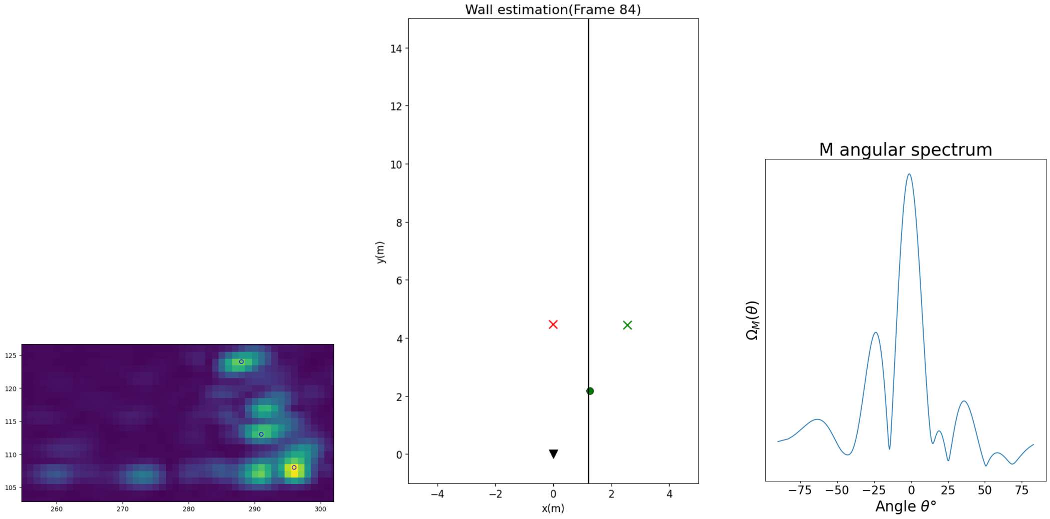

(a) **(b)** **(c)**

Figure 4.6: The figure shows an estimate which was not generated due to the clusters not passing the conditions in section 3.7.2. These results were manually generated. (a) shows a range-Doppler map with the manually selected **T/M/S** marked with circles. (b) shows the wall estimation(green dot) alongside the chosen target position and second order ghost position by the algorithm. (c) shows the angular spectrum of **M**. The second largest peak does not reach over half the amplitude of the largest, resulting in the **T/M/S**-combination being discarded.

4.2 Varying Wall Angle

Here the algorithm was tested with different angles between wall and radar, setups explained in 3.10.2, in addition to the just presented 0° case, referred to as *Single parallel wall*. For each angle the target was walking along the wall with two different distances to the wall, 90 cm and 150 cm, which turned out to have some impact on the results. The results for an increasing angle are presented in the subsequent sections below, followed by a section comparing and discussing the results.

When interpreting the results one should be cautious. This test was intended to try how the algorithm's performance is dependent on the angle between wall and boresight, but there is potentially another phenomenon that must be considered; the occlusion of multipath by the target's body. What this means is that the signal path of the **S**-ghost in the multipath model depicted in figure 2.2 for example, is broken by the body of the target. This could cause no multipath detections to appear, and therefore these wall segments will not be correctly estimated. Note that this is not a phenomenon that has been observed and its appearance quantified, but rather something that would reasonably happen and should be kept in mind when interpreting the results.

4.2.1 Angle of 22.5°

An approximate angle of 22.5° between the wall and the radar direction was used for the results in figure 4.8. The movements for each part is explained in figure 4.7, where the distance to the wall was ~90 cm in the first two, and ~150 cm in the last two parts. In figure 4.8, subfigure (a) and (b), with the target moving closer to the wall, the estimates are marginally noisier compared to with the target further away in (c) and (d). Generally occurring across all the subfigures, are some far off outliers, where the angle has been greatly misestimated. This is seen both by some green crosses, marking the selected **S**-position, being far off to the left in the figures, and by wall estimates being far off to the left as well. These are of course connected to each other, with the **S**-position alongside **T**-position as input when calculating the reflection point in between them. Some of these far off outliers are as far as 300 cm from the wall. But the majority of the estimates are gathered nicely along the wall, supported by that 90% of the estimates lies within a margin of 29 cm from the wall, fetched from the cumulative distribution in (f).

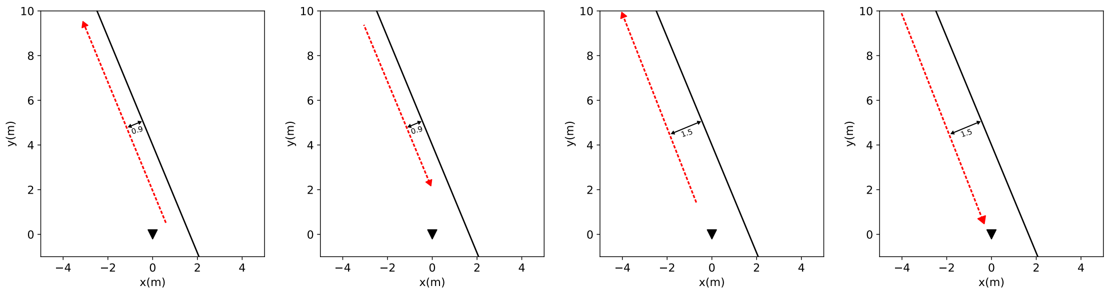

(a) (b) (c) (d)

Figure 4.7: Target movements with angle 22.5° of the sections presented with resulting wall estimates in figure 4.8.

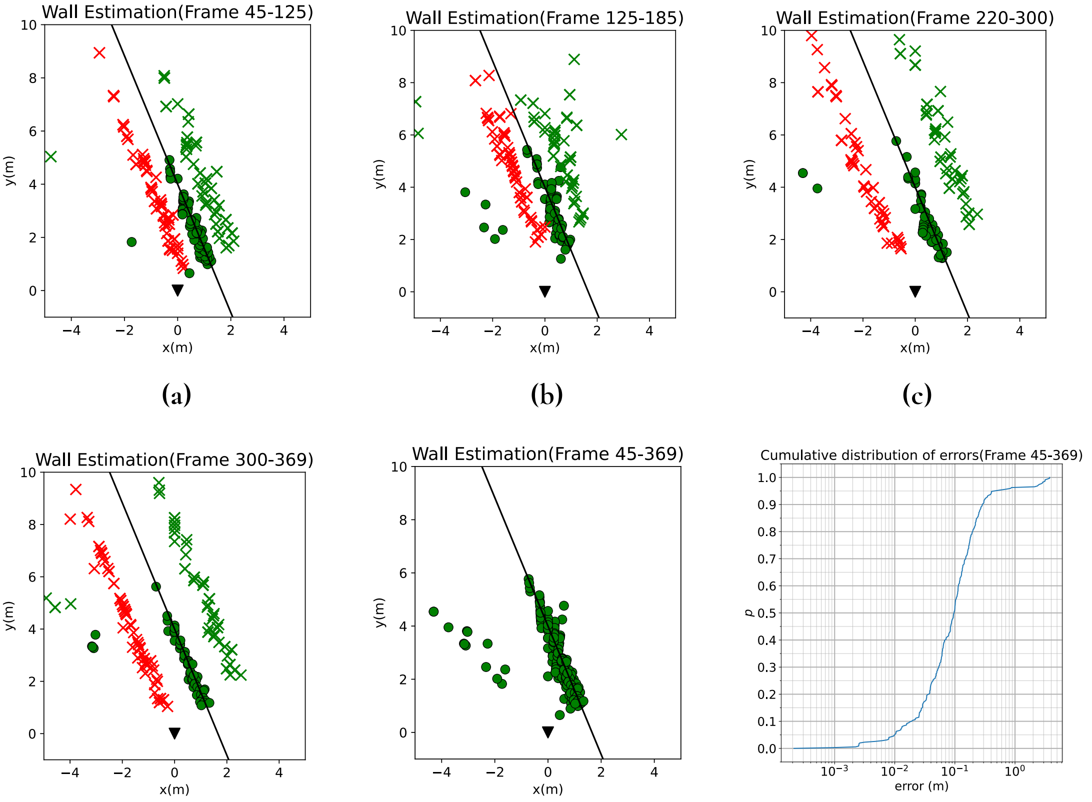

(a) (b) (c)

(d) (e) (f)

Figure 4.8: Wall estimates for a wall with an angle of approximately 22.5° to the radar direction. (a)-(d) are parts of the recording, with movements described in figure 4.7. Red/green crosses mark predicted target/ghost positions. Green dots are the wall estimate points. Black line marks the real wall and the black triangle is the radar, looking in the y-direction. (e) contains the sum of all the parts, with just the wall estimates. (f) is the cumulative distribution of the estimate errors with the x-axes scaled logarithmically.

4.2.2 Angle of 45°

Using an angle of 45° instead, yielded the results in figure 4.10. Movements of each part is visualized in figure 4.9, where first a distance of ~90 cm from target to wall was used and then ~150 cm. In subfigures (a) and (b) of figure 4.10, with the target closer to the wall, the estimates are once again marginally noisier, as for the 22.5° case. The sections with the target further away, subfigure (c) and (d), have the estimates a bit more well centered around the wall. Subfigure (c) does however contain comparably few estimates, not observed previously. These estimates are of high quality though. In total 90% of the estimates lie within a margin of 36 cm, fetched from the cumulative distribution shown in subfigure (f). This value is slightly higher than for the 22.5° case, but still very satisfactory.

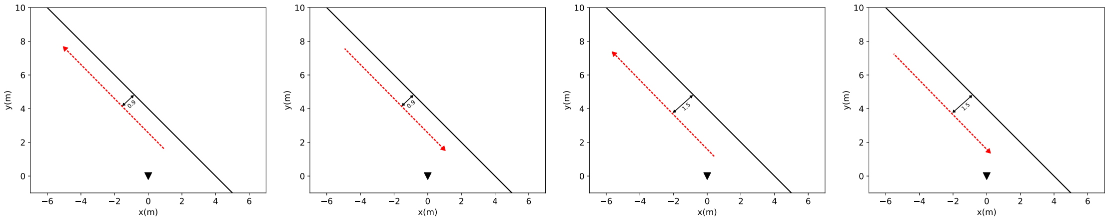

(a) (b) (c) (d)

Figure 4.9: Target movements with angle 45° of the sections presented with resulting wall estimates in figure 4.10.

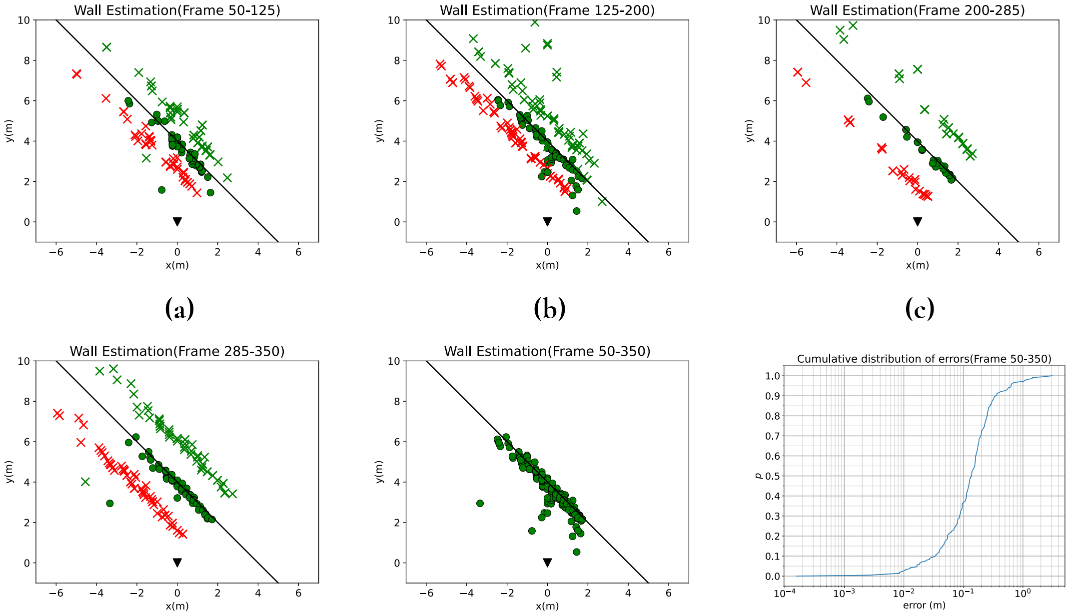

(a) (b) (c)

(d) (e) (f)

Figure 4.10: Wall estimates produced by the algorithm with an angle of 45° between wall and radar. (a)-(d) is showing parts of the recording, with movements explained in figure 4.9. In the figures red/green crosses marks estimated target/ghost positions and the green dots are the wall predictions. The black line is the correct wall and the radar is the triangle at the origin, pointing in the y-direction. (e) contains the sum of all the parts, with just the wall estimates. (f) represents a cumulative distribution of the errors with the x-axes scaled logarithmically.

4.2.3 Angle of 67.5°

Increasing the angle further to 67.5° gave the results in figure 4.12. Movements of each section is seen in figure 4.11, with two distances: ~90 cm and then ~150 cm. Just as the previously presented angles, the target movement closer to the wall seems to yield slightly noisier estimates, comparing subfigure (a)-(b) to (c)-(d) in figure 4.12. The total estimates in (e), can from the cumulative distribution in subfigure (f) be shown to have 90% of the estimates within a distance of 93 cm. This is a significant increase compared to the measurements for the previously presented angles.

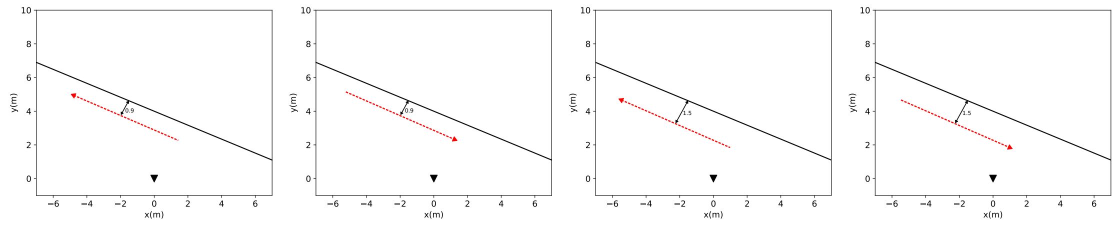

(a) (b) (c) (d)

Figure 4.11: Target movements with angle 67.5° of the sections presented with resulting wall estimates in figure 4.12.

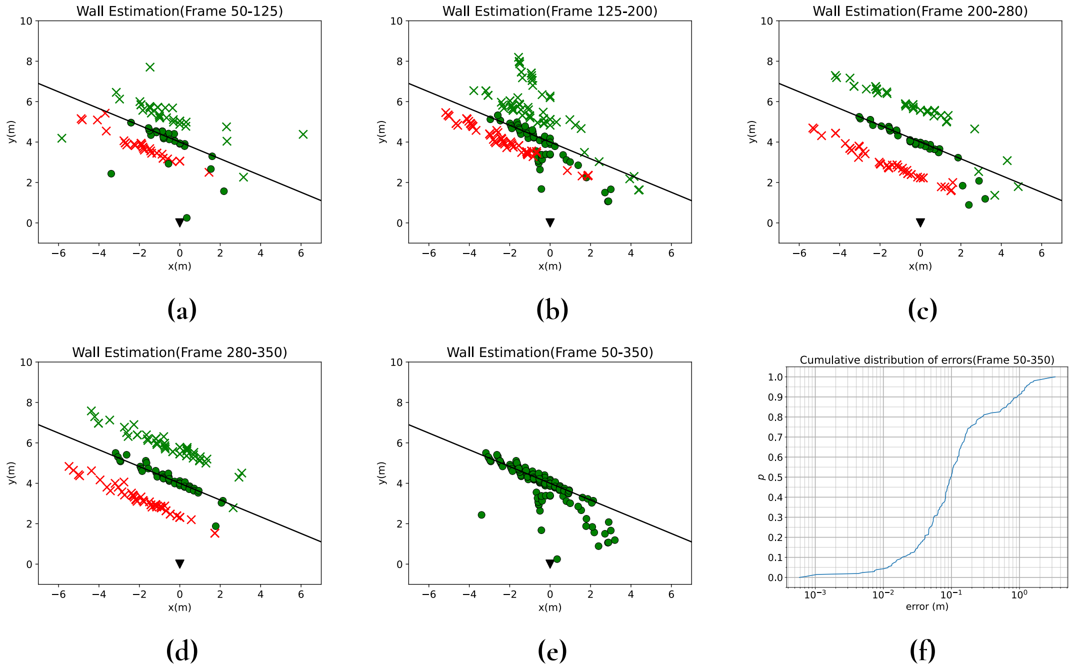

(a) (b) (c)

(d) (e) (f)

Figure 4.12: Wall estimates with an angle of 67.5° between wall and radar. (a)-(d) are the movement sections from figure 4.11). Red/green crosses marks estimated target/ghost positions and green dots marks wall predictions. The black line is the correct wall and the radar is the triangle at the origin, pointing in the y-direction. (e) contains the sum of the recording and (f) represents a cumulative distribution of the errors.

4.2.4 Angle of 90°

Using an angle of 90° between radar and wall yielded the results in figure 4.14. The target movements producing these are explained in figure 4.13, where the initial target/wall distance was ~90 cm, and later ~150 cm. Subfigures (a) and (b) of figure 4.14, with the target closer to the wall, once again display noisier results. The contrast to (c) and (d), with the target further away, is much more distinctive in this setup. Another observation that can be made is that the middle of the wall, right in front of the radar, lacks good estimates. That this is the case across (a)-(d), is also seen in the sum of the estimates in (e), with no good estimates in the middle. From the cumulative distribution of the errors in (f), we can retrieve that 90% of the estimations in this case lie within a margin of 119 cm. This is the largest measurement of the 90th percentile encountered for the varying angle setups.

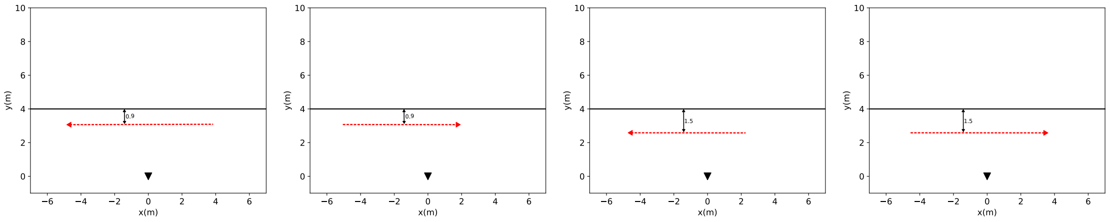

(a) **(b)** **(c)** **(d)**

Figure 4.13: Target movements with angle 90° of the sections presented with resulting wall estimates in figure 4.14.

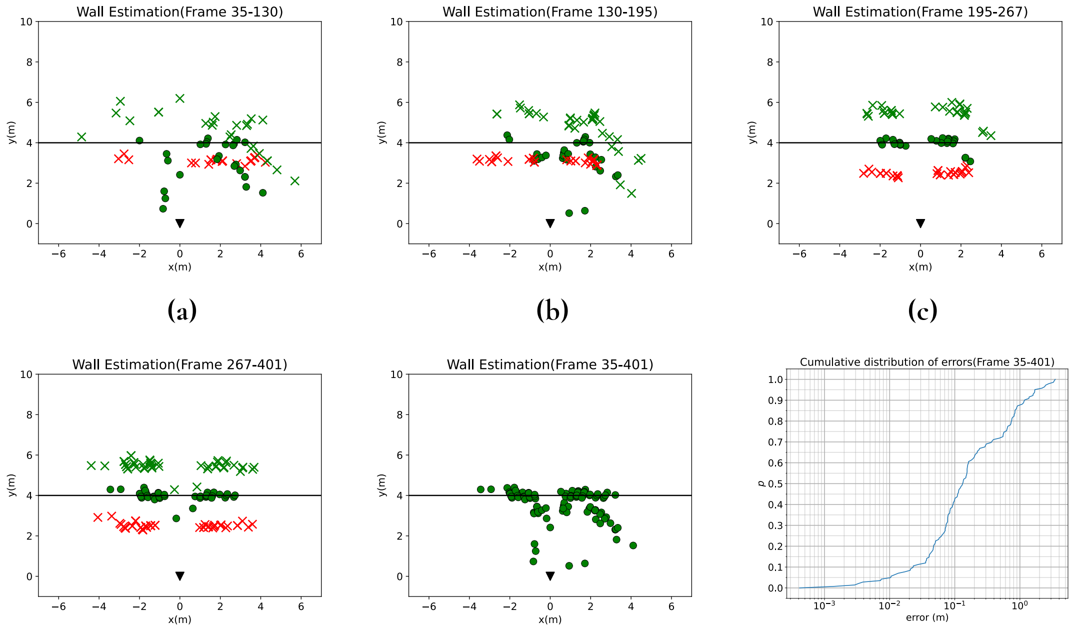

(a) **(b)** **(c)**

(d) **(e)** **(f)**

Figure 4.14: Wall estimates with an angle of 90° between wall and radar. (a)-(d) are the movement sections from figure 4.13). Red/green crosses marks estimated target/ghost positions and green dots marks wall predictions. (e) contains the sum of the recording and (f) represents a cumulative distribution of the errors.

4.2.5 Comparison

Comparing the result of the varying wall angle, we have observed two trends:

- The results get noisier when the wall approaches being perpendicular to the radar direction.
- Walking at a distance of ~150 cm from the wall is easier for the algorithm than ~90 cm.

Starting with the second, one could argue it is a logical find. Increasing the separation between wall and target naturally increases the extra path the multipath signal has to take. This means a greater separation in the range-Doppler map, i.e. less likely that the clusters will overlap and cause trouble for the algorithm.

As for the first one, the largest angles of the setups (67.5° and 90°) has the poorest results, with 90° being the worst. Here one needs to consider that the 67.5° and the 90° cases may have sections of the wall which will be occluded by the body of the target, thereby not allowing multipath reflections. This could possibly prevent these sections to be estimated, and it might allow for estimates with larger errors to slip in. Looking at subfigure (e) in both figure 4.12 and 4.14 there seems to exist such estimates in the vicinity of the sections which may be subject to occlusion.

In table 4.1 some errors from the cumulative distributions are collected. It presents a more nuanced picture. It is indeed so that a larger angle between boresight and the wall leads to a larger error for the 90th percentile. Considering the 50th percentile on the other hand, we can see that the error is not at all continuously increasing with the angle. The same goes for the 75th percentile, where the error is at its largest for 90°, but other than that there is no clear pattern. So this tells us that a big part of the estimations, as much as 75%, are similarly centered around the wall for the tested wall angles, but with the 90° setup being significantly worse. Also, it tells us that with increasing angle the large outliers seem to be worse, leading to a worse 90th percentile. This suggests that some sort of outlier filtering could be useful for the algorithm to better handle difficult wall angles.

Angle\Percentile	**50%**	**75%**	**90%**
22.5°	10 cm	17 cm	29 cm
45°	14 cm	23 cm	36 cm
67.5°	10 cm	19 cm	93 cm
90°	13 cm	63 cm	119 cm

Table 4.1: The table presents the 50th, 75th and 90th percentile of the wall estimation error, for angles 22.5°, 45°, 67.5° and 90°.

4.3 Aluminium vs. No Aluminium

Here the results from setup 3.10.3 is gathered, where we had the same radar position and setup, with and without aluminium foil on the wall. Figure 4.15 shows the target movement for the foil case, as reference. The corresponding wall estimates produced by our algorithm is showed in figure 4.16. As can be seen, the algorithm produces a reasonable amount of estimates. With the foil off, the target movements was as in figure 4.17, identical to before. The produced estimates can be found in figure 4.18. Clearly the number of estimates are very few in comparison.

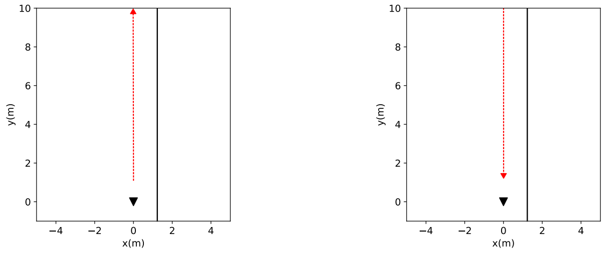

(a) Frame 63-147

(b) Frame 147-245

Figure 4.15: Movement of the target in recording with foil on the wall. The wall is marked with a black line. Wall estimates produced by these movements can be found in figure 4.16.

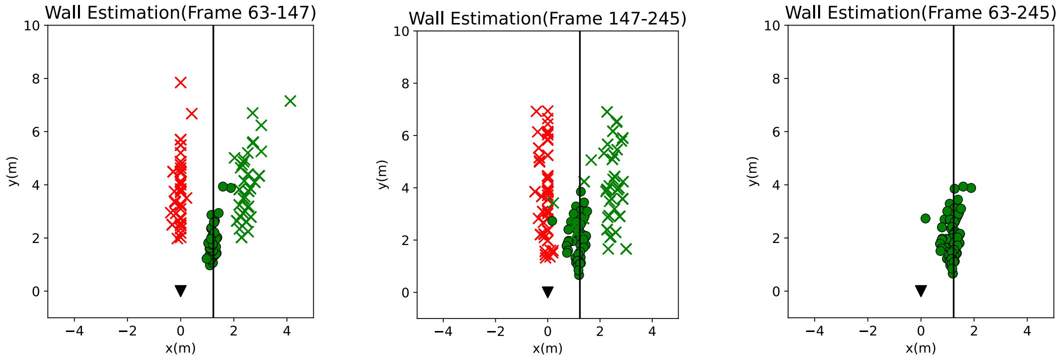

(a) **(b)** **(c)**

Figure 4.16: Wall estimates for recording with aluminium on the wall. Radar marked with a black triangle and looking in the y-direction. The black line marks the real wall. (a) and (b) contains wall estimates using the second order ghost. The predicted target positions(red crosses) and second order positions(green crosses) producing the estimates are included. How the target moved in the two sections is seen in figure 4.15. (c) contains the sum of the estimates in (a) and (b), with the target/ghost positions filtered out.

As mentioned before, radar reflects very well off of metallic surfaces compared to regular indoor walls. This was confirmed pretty early during the thesis process, by simply examining the range-Doppler maps. It could be seen that the nice linear pattern, discussed in section 2.3, appeared much more clear and frequent when the walls were covered in part with a sheet of aluminium foil. This became even more evident when comparing how well our algorithm

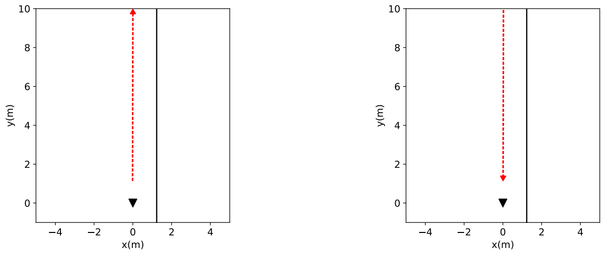

(a) Frame 50-147

(b) Frame 147-250

Figure 4.17: Movement of the target in recording without foil on wall. The wall is marked with a black line. Wall estimates produced by these movements can be found in figure 4.18.

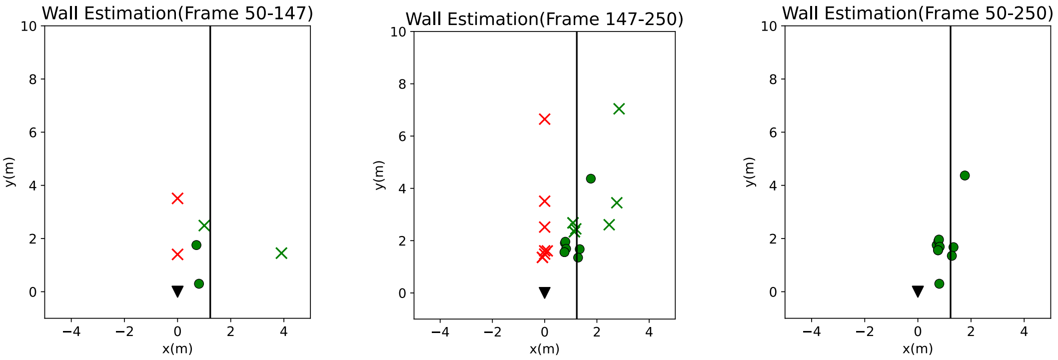

(a) **(b)** **(c)**

Figure 4.18: Wall estimates from recording without aluminium foil on wall. The wall estimates are marked with bordered green dots and the black line is the real wall. The target positions(red crosses) and second order ghost positions(green crosses) for the frames producing wall estimates are also included. (a) and (b) are sections of the recording where the target moved away from the radar and towards respectively, as seen in 4.17. (c) contains the sum of the wall estimates for both (a) and (b) with the target/ghost positions filtered out.

performed. Without the foil, very few wall estimations were produced(figure 4.18), compared to with it added(figure 4.16). One should remember however that the algorithm's lack of usefulness in scenes where multipath is not as prevalent, is not an argument against the algorithm's usefulness in general. This since, the main reason for identifying multipath and recreating the reflective surface is due to wanting to suppress it, and if there is no multipath, there is not an issue. The indoor environment with aluminium added was just used as a controlled environment, imitating scenes where multipath reflections are very prevalent.

4.4 Tunnel

The results from the *Tunnel* setup is shown in figure 4.20, where as a reference the target movements for the sections are included in figure 4.19. For the sections(4.20a-4.20c), the target positions and second order ghost positions that produced the estimates are also visualized, while the sum(4.20d) just contains the estimates.

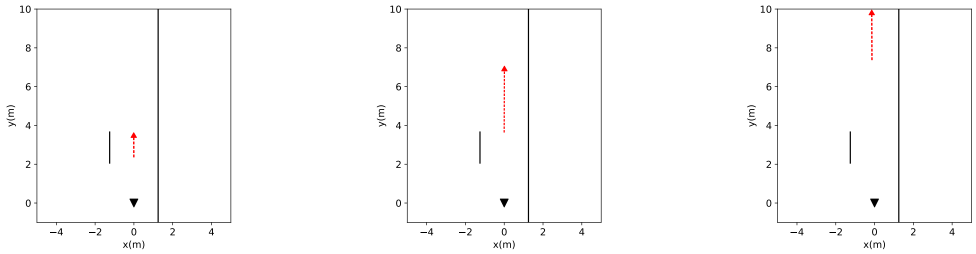

(a) Frame 50-67

(b) Frame 67-92

(c) Frame 92-120

Figure 4.19: Target movements of the sections presented with resulting wall estimates in figure 4.20.

The developed algorithm was hypothesized to have a hard time with the *Tunnel* setup. This because, as mentioned before, more angles of interest should be present in the range-Doppler bins chosen as ghost positions by the algorithm. The reason being, that reflections off of respective side of the "tunnel" travel the same distance, with the target in the middle of the tunnel, and hence end up in the same range-Doppler bin, but with the angles of respective side of the tunnel. The algorithm was designed to only have to handle two angles per bin, the reflection angle and target angle. In this setup there is potential for three, target angle and the two angles from respective side of the tunnel. In figure 4.20 it is observed however that the algorithm performed relatively well. Wall estimates were produced in numbers on both sides of the tunnel, although with a significant gap in the middle of the screen side. After further investigation, single frames were found with simultaneous estimates on both sides, contrary to our hypothesis. An example of this is seen in figure 4.21. The reason behind this was discovered to be that three different clusters were considered as second order, being the furthest away cluster, see figure 4.21b. These clusters had different angle information, most with the angle of the long wall, but one with the angle of the screen on the other side. Hence resulting in estimations on both sides for a single frame. In other words, although a single

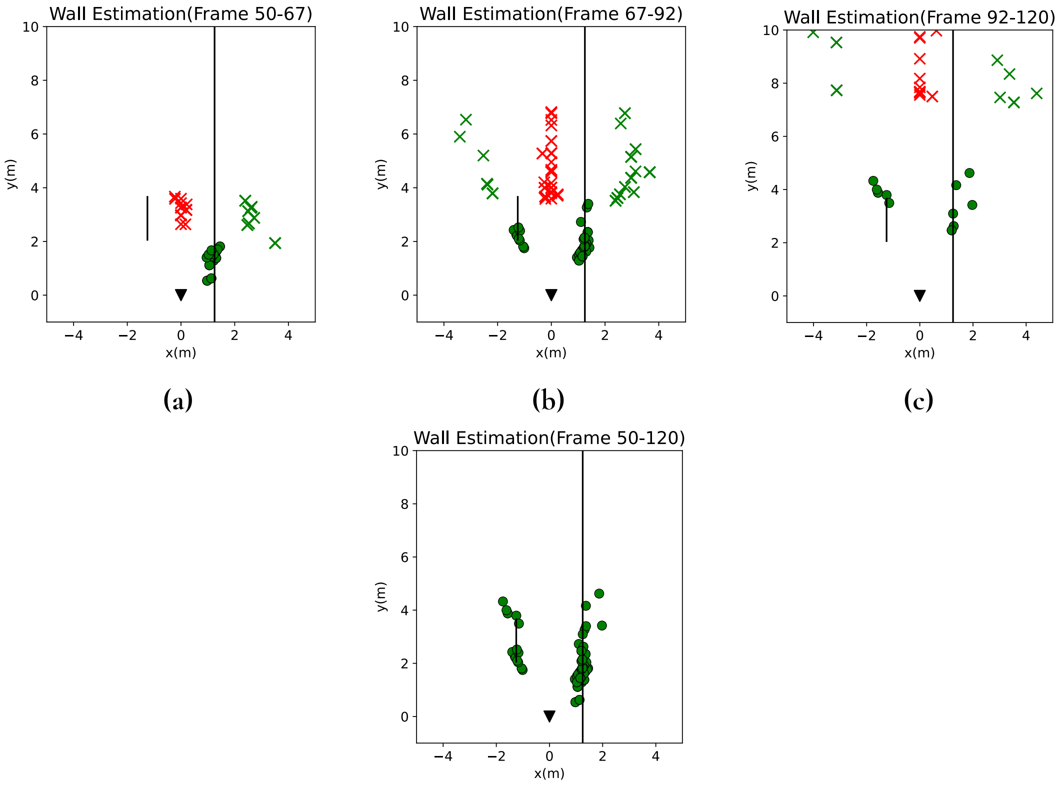

(a) (b) (c)

(d)

Figure 4.20: Wall estimates from the *Tunnel* setup. The radar is at the origin marked with a black triangle, and pointing in the y-direction. The black lines are wall/screens covered in part with aluminium. The green dots are wall estimates produced by target positions(red crosses) in combination with second order ghost positions(green crosses). (a)-(c) Subtotals of the wall estimates, with target and second order ghost positions included. Movements for these shown in figure 4.19. (d) Total wall estimates from (a)-(c), but with target/ghost positions filtered out.

found Hough line, with possible **T**, **M** and **S**, only can estimate one side of the tunnel, the fact that we process the other found lines too, makes it possible to get estimates on both sides in a single frame.

So the conclusion from the *Tunnel* setup is that the algorithm can handle more delicate geometries than just a straight wall. It also suggests that by not restricting the algorithm to one ghost position, but to use many possible ones for the estimation, reflections off of several reflectors have the potential to be discovered on a per frame basis, like indicated in figure 4.21.

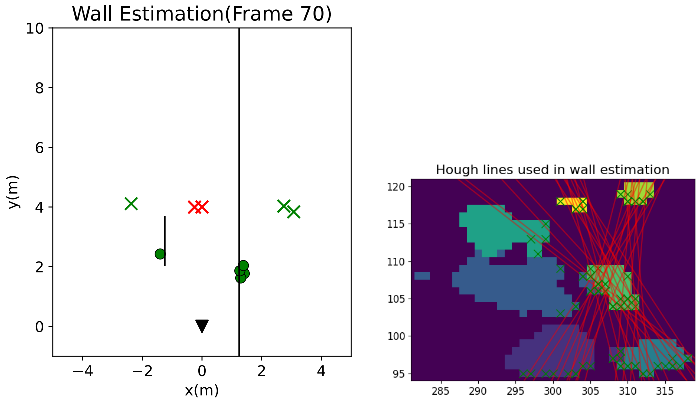

(a) **(b)**

Figure 4.21: Example of a single frame that yielded wall estimates on both sides of the "tunnel". (a) contains the wall estimates. Black lines are walls in the scene(with aluminium added), the black triangle is the radar position(pointed in y-direction) and red/green crosses are predicted target/ghost(second order) positions used for the estimates, that are marked with green dots. (b) shows a range-Doppler view with the clusters and Hough lines(red lines), in combination with the points on the lines fulfilling our linear relationship(green crosses), used in the estimation. In this case we end up with three different second order candidates, the clusters furthest away with line going through. These have different angle information, which is the reason we get estimates on both sides in (a).

4.5 The L

Subfigures (a)-(d) in figure 4.23 shows the resulting second order wall estimates for the L setup. Each subfigure represents a portion of the video, presented more detailed in figure 4.22. Along with the estimates, the targets and second order ghosts that created said estimates are also plotted in red and green crosses, respectively. In subfigure (e) the total accumulation of second order wall estimates are presented, i.e. the sum of subfigures (a)-(d).

In the data set there are two reflective surfaces present: The wall, as well as an additional wall composed of two screens which are, like the wall, covered by a sheet of aluminium foil. The shorter of the walls will be referred to as the screens, while the other will simply be referred to as the wall. The purpose of the setup was to investigate how the algorithm would deal with two separate reflective surfaces with very different angles in relation to the camera that are present in the same frame. The direction of the walk was orthogonal in subfigure (a) and (d), compared to (b) and (c).

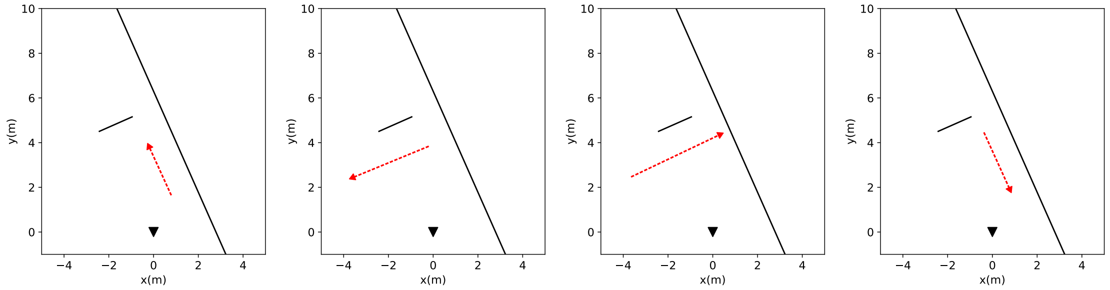

(a) Frame 59-75

(b) Frame 76-108

(c) Frame 109-160

(d) Frame 161-195

Figure 4.22: Target movements of the sections presented with resulting wall estimates in figure 4.23.

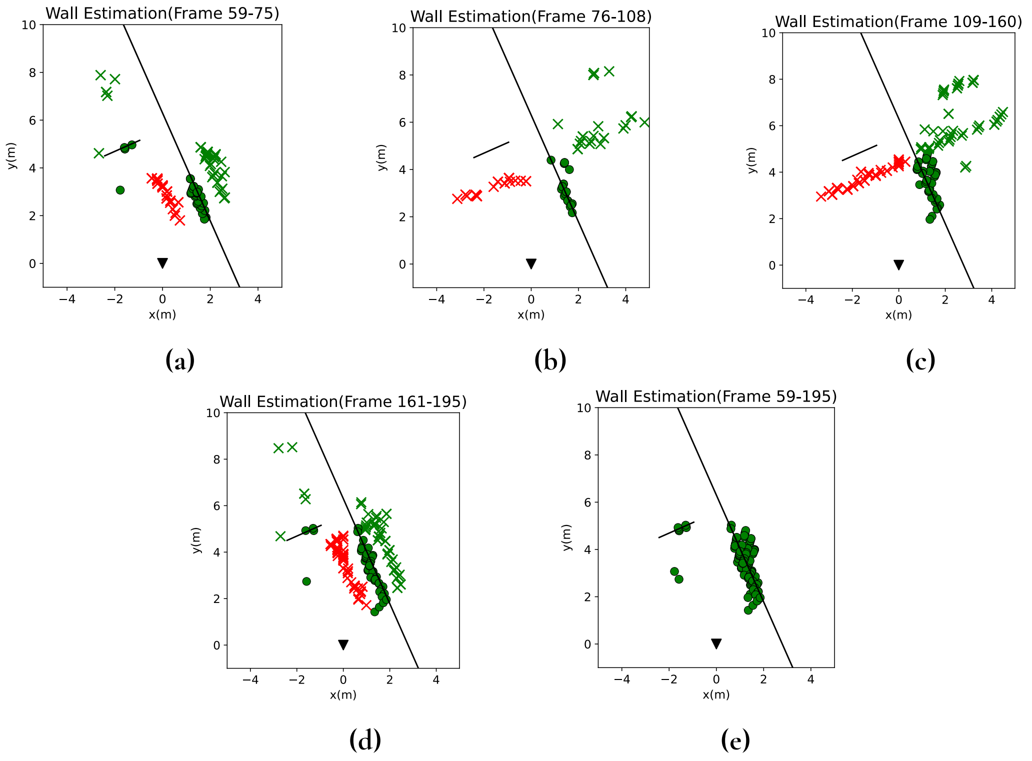
Wall Estimation(Frame 59-75)

Wall Estimation(Frame 76-108)

Wall Estimation(Frame 109-160)

Wall Estimation(Frame 161-195)

Wall Estimation(Frame 59-195)

Figure 4.23: The red and green crosses are the targets and second order ghosts respectively, which contributed with a wall estimate. The green points are the aforementioned wall estimates. The black lines are walls and screens clad in aluminium. The black triangle is the radar position, pointing in the y-direction. (a)-(d) contain parts of the recording, with target movements in figure 4.23 and (e) is the sum for all the movements.

Subfigures (a) and (d) in figure 4.23 correspond to the target walking along the same path in opposite directions. The overall result is satisfactory with the bulk of the estimations following the wall well. There is some noise, especially when the target approaches the radar in subfigure (d). Overall there is minimal noise. The screens are not as well covered as the wall but there is a handful of points in both (a) and (d), correctly placed on the screens. In figure 4.24 a frame that produces both a screen estimate and a wall estimate is seen. Subfigure (c) depicting the clustered detections also contains two lines, a red line which yields the wall estimate, and a green line which yields the screen estimate. This frame renders even more robustness to the algorithm, showing it is capable of more difficult geometries than just straight, plane walls.

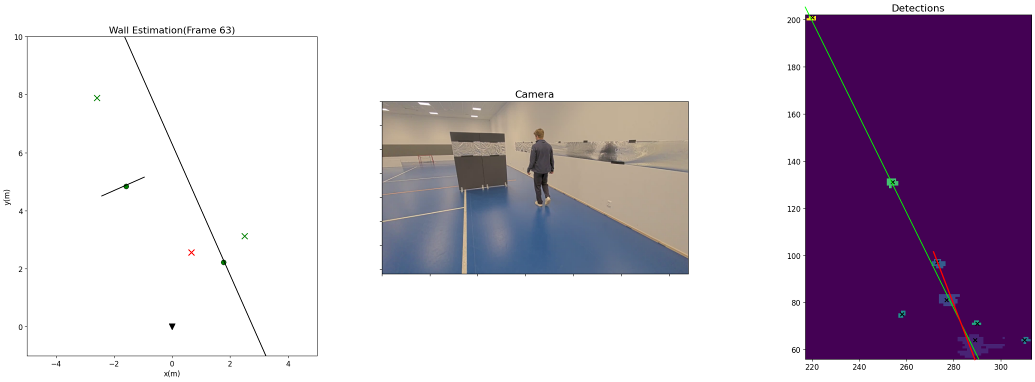

(a) **(b)** **(c)**

Figure 4.24: The results of frame 63 in the L-setup. Subfigure (a) contains the wall and the screens depicted with black lines, the radar as a black triangle, the target as a red cross, the second order ghosts are plotted as green crosses, and the wall estimates as green circles. Subfigure (b) contains the camera picture. Subfigure (c) depicts the clustered detections, as well as two lines marking the cluster combinations that generated the wall estimates. The green line generated the estimate on the screens, and the red line the estimate on the wall.

Subfigures (b) and (c) in figure 4.23 likewise correspond to the target walking the same path in opposite directions. Both subfigures have in common that no estimations are present on or near the screens. It appears that the algorithm performs poorly when the target is walking in front of the screens. Some reasons for this may be:

- The target may block any potential first or second order ghost with its body.
- The movement of the target is not in a radial direction to the radar, i.e. the Doppler speed is very small, making it hard to cluster.

The overall distribution of wall estimates is on the whole satisfactory. The wall gets well covered and the position of the screens might be determined with a higher degree of security with more data on this setup.

4.6 First Order vs. Second Order

With background of the theory in section 2.6 about the bistatic issue, we suspected that using the combination target/first order would yield much poorer results than target/second order. According to the theory the angle estimation for the first order ghost(DoD ≠ DoA) is expected to be unreliable and noisy. Second order estimates is what we have presented in the previous sections. But here we compare a handful of the setups to using first order instead. Figure 4.25 compares the standard setup and figures 4.26-4.29 compare with the different angles used.

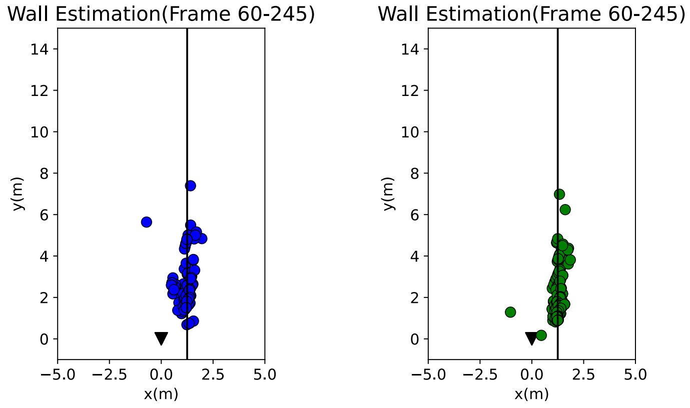

(a) (b)

Figure 4.25: Comparison between estimations using identified **T/M**-positions in (a) and **T/S**-positions in (b) for the *Single parallell wall* setup. The line is the real wall and the radar(triangle) is placed at the origin directed in the y-direction.

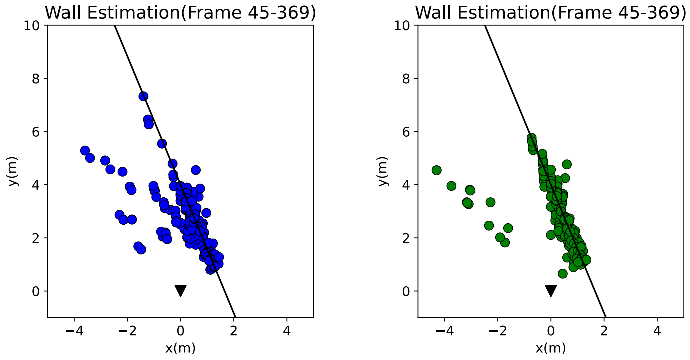

(a) (b)

Figure 4.26: Comparison between estimations using identified **T/M**-positions in (a) and **T/S**-positions in (b). The angle between radar boresight(y-direction) and wall is 22.5°. The line is the real wall and the radar(triangle) is placed at the origin.

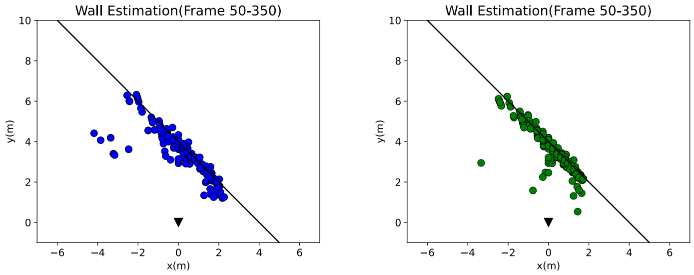

(a) **(b)**

Figure 4.27: Comparison between estimations using identified **T/M**-positions in (a) and **T/S**-positions in (b). The angle between radar boresight(y-direction) and wall is 45°. The line is the real wall and the radar(triangle) is placed at the origin.

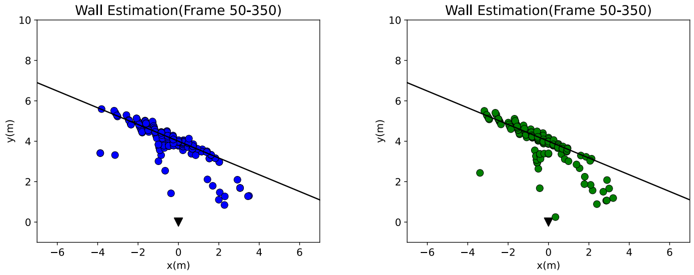

(a) **(b)**

Figure 4.28: Comparison between estimations using identified **T/M**-positions in (a) and **T/S**-positions in (b). The angle between radar boresight(y-direction) and wall is 67.5°. The line is the real wall and the radar(triangle) is placed at the origin.

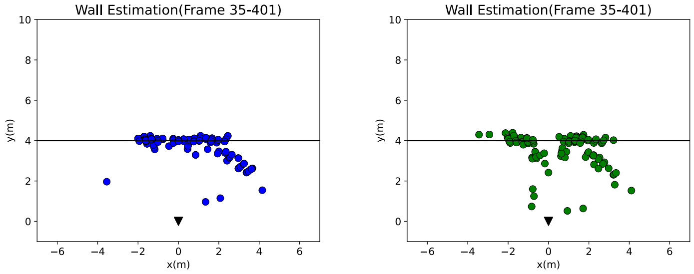

(a) **(b)**

Figure 4.29: Comparison between estimations using identified **T/M**-positions in (a) and **T/S**-positions in (b). The angle between radar boresight(y-direction) and wall is 90°. The line is the real wall and the radar(triangle) is placed at the origin.

Our hypothesis was, as mentioned before, that the estimates using target/first order would be poorer than using target/second order. This because the angle of signals with different direction of departure and direction of arrival, is difficult to reliably estimate. This issue is named the *bistatic problem* and explained in section 2.6. When examining the results we get some confirmation of this, but the results are not as bad as one might expect. One surprising case even exists, where the results are arguably better with first order compared to second order(figure 4.29). This is the setup with an angle of 90° between radar direction and wall. When investigating varying wall angle this was shown to be a very demanding case. An interesting observation is that it performs significantly better on the segment in the center of the wall, around boresight of the radar. When the target moves here it is logical to think that it would cover the part of the wall that might cause ghost reflections. This is observable in the second order case(fig. 4.29b). There we see a clear gap of about 1m in the center completely lacking estimations close to the real wall. This is not present when using first order however(fig. 4.29a). The most probable explanation is due to the bistatic problem. Figure 4.30 shows the zone on the wall unreachable by the signal. No reflections should be occurring here, since the target is in the way of the signal. An illustrative path of a first order reflection is marked in the figure, where the direction-of-departure(DoD), marked with θ_1 in the figure, is in the direction of the unreachable zone. After reflection of the target it reflects on the wall outside the zone and returns to the radar after the reflection, i.e. with a direction-of-arrival(DoA) outside the unreachable zone. This is the angle we attempt to estimate with the radar. The difference in DoD and DoA distorts the phase in the virtual array, used for the angle estimation, resulting in a noisy estimation. This is what is referred to as the bistatic problem. This distortion results in a possibility of the DoA to be estimated as the DoD instead. In other words, thinking that the signal returned with an angle θ_1, from the unreachable zone, when in reality it was only transmitted in that direction. With this reasoning, the better performance in the center is likely more credited to a wrongly estimated angle, than an intended advantage. The better performance is an unintended coincidence in this case.

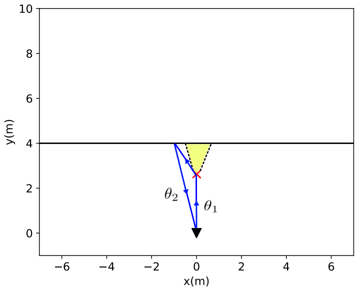

Figure 4.30: Situation with target straight in front of the radar, resulting in a zone unreachable by the signal. Illustration of a first order reflection, with a DoD of θ_1 and DoA of θ_2. This mix of angles compared to the second order case(DoD=DoA) results in the possibility of getting estimations in the unreachable zone, because θ_1 can be present in the signal's angle spectra.

Looking at the other cases, the performance in one of them(angle 67.5°) is pretty similar when comparing first/second. In all the other ones(0°, 22.5°, 45°) second order performs better. The estimates are more centered around the real wall, with less outliers. Since the algorithm needs to find all three, target and the two ghosts, their is no obvious reason to use first order. Naturally, second order signals travels a longer path, and hence are weaker. In other words they are less prevalent in frames. First order could be of use when not finding the second order. In that case you would need another way of identifying the ghosts however. The straight line between the three clusters, with equal distances, is obviously inapplicable when just looking for two.

With background of the bistatic problem, explained in 2.6, we can at least conclude from these comparisons that the problem doesn't make the information in the first order ghosts useless. There is valuable information to gain from them, at least in the scenarios examined in this thesis. In order to further understand when the bistatic problem is more of an issue it needs to be investigated further.

4.7 Effect of Bistatic Problem on Model Performance

Throughout the thesis we have hinted to the bistatic problem being a hindrance in the algorithm. As explained in the *Method*, the bistatic problem was not known to us when much of the algorithm was designed, which explains why the angular spectrum is used without restraint.

Even though most of the wall estimations are done with target and the second order ghost, the angular information of the first order ghost will still have an impact on these estimations. The conditions on the cluster peaks defined in section 3.7.2 of the method, use the first order angle in order to discard and accept combinations of cluster peaks. Before seeing the results presented in the previous section it is therefore hard to know what to expect when you only know of the theory and the algorithm.

When seeing the results we can conclude that the existance of the bistatic problem did not completely foil the performance of the algorithm presented in this thesis. We can see in the results that the estimations often track the real wall well. From the simulation results in section 2.6 we can see that the angular information of the first order ghosts is not always of poor quality. It could be the case that the conditions presented in section 3.7.2 filters out many of the **M**-clusters of poor quality. The fact that the wall estimation results which were done with the target and the first order ghost performed reasonably well seems to indicate that.

4.8 Future Work

In this thesis we have presented a promising algorithm, applicable to UWB-radar. There are however a couple of areas where we have identified possible future improvements and applications.

4.8.1 Adopt to non-UWB

When starting the process of this thesis we used a non-UWB radar, with lower bandwidth and hence lower range resolution, see equation 2.4. We realized quickly however, by examining the range-Doppler images, that the ghost clusters were overlapping too much to clearly distinguish three separated clusters on a straight line. This motivated the transition to UWB-radar, where the separation could be seen. The trade-off with UWB-radar is a decreased max range, in our case being around 21 m. The max range is inversely proportional to the bandwidth, $r_{max} \propto \frac{1}{B}$. In other words with a non-UWB system you can see further, making it suitable for larger geometries. For the algorithm to work in these larger geometries an adoption to handling non-UWB data would be needed. The observed challenge of overlapping clusters would have to be solved in some manner.

4.8.2 Using First Order Only

As briefly mentioned in the discussion comparing first order and second order, an algorithm not needing to find second order ghosts could possibly be more robust. This due to second order signals being much weaker, and hence less frequently occurring. The bulk of the thesis was done in very ideal circumstances, with added aluminium on walls to enhance reflections. In more realistic scenarios, with not as reflective surfaces, relying on finding both first and second order ghosts might not be as reasonable. Another way of identifying the ghosts will be needed though, with just two points there is no linear relationship to search for. The very noisy angle estimation of first order ghosts will have to be addressed as well. This thesis indicates that there is valuable information in the first order ghosts at least, worthy of investigating further. A similar solution to the DNN **M1/M2** classifier[7], as Feng et. al. has created might be useful. The challenge is then if you have several targets, to identify which target belongs to which multipath detection.

Another potentially useful article for this purpose is *Automotive MIMO radar angle estimation in the presence of multipath* by F. Engels et. al.[26]. If only the first order is used, the bistatic problem needs to be addressed in order to actually use the angular information. In the article by F.Engels et. al. a signal model is presented which contain either two targets or a target in the presence of multipath. F. Engels et. al. then presents maximum likelihood estimators for the angle, for both the two target signal model and the target in the presence of multipath. A generalized likelihood ratio test (GLRT) is used to determine which of the signal models to use. A similar system may be added to the algorithm implemented in this thesis. Once a cluster has been identified as first order multipath, a maximum likelihood estimator could potentially be able to better resolve the angular composition of the signal.

4.8.3 Adding Elevation

This thesis has been restricted to just deal with the horizontal angle(azimuth) information. By adding elevation information, their is potential to expand the solution to mapping reflective 3D-surfaces. Adding another dimension will surely introduce further complexity and challenges. We observed that the estimation yielded a bit poorer results when the target walked closer to the wall, comparing a distance of 90 cm to 150 cm. In the 3D-case one of the reflective surfaces, the floor, will always be in contact with the person walking, i.e. no distance in between target and reflector. This might possibly make the estimation of the floor more difficult. The target, at least if it is a standing person, does however cover space from the floor and a decent distance up from the floor, also producing reflections. Therefore reflections off parts further from the floor might contribute to a good estimation.

Chapter 5

Conclusion

We have in this thesis developed an algorithm that is able to recognize multipath detections as well as estimate a position of the reflective surface, and we have determined that it is realistic to use the algorithm on real data. The results produced range from very accurate, to less accurate and more noisy. The accuracy of estimations depends on the geometry of the scene as well as the path taken by the target.

When it comes to the dependency on the geometry, our results indicate that the angle separating the boresight and the angle of the wall may affect the prevalence of wall estimates. The results indicate that for a wall which is less aligned with the boresight, meaning that the angle between the two is large, there may be wall estimates with a large error. Unfortunately the amount of occlusion between the target and wall was unintentionally varied significantly between the differing angle setups. Therefore further investigation, just varying angle independently of amount of occlusion, would be needed to draw stronger conclusions. The path taken by the target has not been as thoroughly investigated, but one finding is that the distance of the target from the wall impact the results, with better results for a distance of 150 cm compared to 90 cm.

The algorithm shows promise in dealing with scenes with multiple reflective surfaces at once. Two parallel walls, forming a tunnel, yielded decent estimates on both sides. This was also the case for two perpendicular walls, forming an L. For these scenarios the estimations were a bit more sparse in some areas. With more data these areas could potentially be filled.

We suspected that the bistatic problem would impact the estimations from first order ghosts negatively. The results presented in the thesis seem to confirm that suspicion. The results are in general better for the second order estimations, but not as significantly as suspected. Before deciding whether the bistatic problem causes enough problems to warrant a thorough solution, the prevalence of this issue needs further investigation.

The algorithm shows promise and could potentially be used in the future to identify multipath detections. With more knowledge of the geometry of a room, provided by the algorithm, it might be possible to filter out the ghost tracks of a scene.

References

[1] P. Setlur, M. Amin, and F. Ahmad, "Multipath model and exploitation in through-the-wall and urban radar sensing," *IEEE Transactions on Geoscience and Remote Sensing*, vol. 49, no. 10, pp. 4021–4034, 2011.

[2] Wikipedia, "Ray tracing (physics)." `https://en.wikipedia.org/wiki/Ray_tracing_(physics)`, Accessed: 2023-05-15.

[3] A. Kamann, P. Held, F. Perras, P. Zaumseil, T. Brandmeier, , and U. T. Schwarz, "Automotive radar multipath propagation in uncertain environments," *21st International Conference on Intelligent Transportation Systems (ITSC)*, 2018.

[4] K.-P.-H. Thai, O. Rabaste, J. Bosse, D. Poullin, I. D. H. Saenz, T. Letertre, and T. Chonavel, "Detection–localization algorithms in the around-the-corner radar problem," *IEEE Transactions on Aerospace and Electronic Systems*, vol. 55, 2019.

[5] F. Kraus, N. Scheiner, W. Ritter, and K. Dietmayer, "Using Machine Learning to Detect Ghosts Images in Automotive Radar," 2007. Mercedes-Benz AG, 70565 Stuttgart, Germany & Institute of Measurement, Control and Microtechnology, Ulm University, 89081 Ulm, Germany.

[6] R. Feng, E. D. Greef, M. Rykunov, H. Sahli, S. Pollin, and A. Bourdoux, "Multipath Ghost Recognition for Indoor MIMO Radar," *IEEE Transactions on Geoscience and Remote Sensing*, vol. 69, 2022.

[7] R. Feng, E. D. Greef, M. Rykunov, H. Sahli, S. Pollin, and A. Bourdoux, "Multipath ghost classification for mimo radar using deep neural networks," 2022.

[8] W. Klembowski, A. Kawalec, and W. Wizner, "Passive radars as sources of information for air defence systems," *Passive Radar, Challenges Concerning Theory and Practice in Military Applications*, 2013.

[9] F. Engels, P. Heidenreich, M. Wintermantel, L. Stäcker, M. A. Kadi, and A. M. Zoubir, "Automotive Radar Signal Processing: Research Directions and Practical Challenges," *IEEE Journal of Selected Topics in Signal Processing*, vol. 15, no. 4, 2021.

[10] J. Bai, S. Li, H. Zhang, L. Huang, and P. Wang, "Robust target detection and tracking algorithm based on roadside radar and camera," *Sensors*, vol. 21, 2021.

[11] Y. Jin, B. Kim, S. Kim, and J. Lee, "Design and implementation of fmcw surveillance radar based on dual chirps," *Elektronika Ir Elektrotechnika*, vol. 24, no. 6, 2018.

[12] V. M. Milovanovic, "On Fundamental Operating Principles and Range-Doppler Estimation in Monolithic Frequency-Modulated Continuous-Wave Radar Sensors," *Electronics and Energetics*, vol. 31, 2018.

[13] S. Suleymanov, "Design and implementation of an fmcw radar signal processing module for automotive applications," Master's thesis, University of Twente, Enschede, Netherlands, Aug. 2016.

[14] V. Winkler, "Range doppler detection for automotive fmcw radars," *Proceedings of the 4th European Radar Conference*, 2007.

[15] S. Rao, "MIMO Radar," tech. rep., Texas Instruments, July 2018. `https://www.ti.com/lit/an/swra554a/swra554a.pdf?ts=1678191672970`, Accessed: 2023-04-12.

[16] M. M. Vázquez, "Basics of fmcw radar." `https://www.renesas.com/us/en/blogs/basics-fmcw-radar`, 2021. Accessed: 2023-05-09.

[17] Wikipedia, "Hough transform." `https://en.wikipedia.org/wiki/Hough_transform#cite_note-1`, Accessed: 2023-04-12.

[18] K. Bapat, "Hough transform with opencv (c++/python)," 2019. `https://learnopencv.com/hough-transform-with-opencv-c-python/`, Accessed: 2023-04-12.

[19] G. Seif, "The 5 clustering algorithms data scientists need to know." `https://towardsdatascience.com/the-5-clustering-algorithms-data-scientists-need-to-know-a36d136ef68`, 2018. Accessed: 2023-05-09.

[20] M. Ester, H.-P. Kriegel, J. Sander, and X. Xu, "A density-based algorithm for discovering clusters in large spatial databases with noise," *Proceedings of the Second International Conference on Knowledge Discovery and Data Mining (KDD-96)*, 1996. Institute for Computer Science, University of Munich.

[21] S. Sun, A. P. Petropulu, and H. V. Poor, "Mimo radar for advanced driver-assistance systems and autonomous driving: Advantages and challenges," *IEEE Signal Processing Magazine*, 2020.

[22] M. A. Richards, *Fundamentals of Radar Signal Processing*, ch. 6.5.6, pp. 354–357. McGraw-Hill Education, second ed., 2005.

[23] R. L. Burden and J. D. Faires, *Numerical Analysis*, ch. 2.1. PWS Publishers, third ed., 1985.

[24] E. Coca and V. Cehan, “Laboratory study of electromagnetic waves reflectivity of certain materials,” *Proceedings of the 2014 37th International Spring Seminar on Electronics Technology*, 2014.

[25] C. Wolff, “The radar range equation.” `https://www.radartutorial.eu/01.basics/The%20Radar%20Range%20Equation.en.html`. Accessed: 2023-05-10.

[26] F. Engels, M. Wintermantel, and P. Heidenreich, “Automotive MIMO Radar Angle Estimation in the Presence of Multipath,” *Proceedings of the Second International Conference on Knowledge Discovery and Data Mining (KDD-96)*, 2017. Institute for Computer Science, University of Munich.